

# On-Demand Selection of the Latent Domain Orientation in Spray-Deposited Block Copolymer Thin Films

S. Cetindag, G. Doerk

To be published in "ACS Nano"

January 2025

Center for Functional Nanomaterials  
**Brookhaven National Laboratory**

**U.S. Department of Energy**

USDOE Office of Science (SC), Basic Energy Sciences (BES). Scientific User Facilities (SUF)

Notice: This manuscript has been authored by employees of Brookhaven Science Associates, LLC under Contract No. DE-SC0012704 with the U.S. Department of Energy. The publisher by accepting the manuscript for publication acknowledges that the United States Government retains a non-exclusive, paid-up, irrevocable, world-wide license to publish or reproduce the published form of this manuscript, or allow others to do so, for United States Government purposes.

## **DISCLAIMER**

This report was prepared as an account of work sponsored by an agency of the United States Government. Neither the United States Government nor any agency thereof, nor any of their employees, nor any of their contractors, subcontractors, or their employees, makes any warranty, express or implied, or assumes any legal liability or responsibility for the accuracy, completeness, or any third party's use or the results of such use of any information, apparatus, product, or process disclosed, or represents that its use would not infringe privately owned rights. Reference herein to any specific commercial product, process, or service by trade name, trademark, manufacturer, or otherwise, does not necessarily constitute or imply its endorsement, recommendation, or favoring by the United States Government or any agency thereof or its contractors or subcontractors. The views and opinions of authors expressed herein do not necessarily state or reflect those of the United States Government or any agency thereof.

# On-Demand Selection of Latent Domain Orientation in Spray Deposited Block Copolymer Thin Films

*Semih Cetindag* †, *Beatrice Bellini* † $\perp$ , *Ruipeng Li* ‡, *Esther H.R. Tsai* †, *Dmytro Nykypanchuk* †, *Gregory S. Doerk* †\*

† Center for Functional Nanomaterials, Brookhaven National Laboratory, Upton, NY 11973, USA.

‡ National Synchrotron Light Source II, Brookhaven National Laboratory, Upton, NY 11973, USA.

$\perp$  Columbia University Department of Chemical Engineering, New York, NY 10027, USA.

KEYWORDS. Nanofabrication, block copolymer thin films, morphology, domain orientation, spray deposition, droplet evaporation.

ABSTRACT.

With their ability to self-assemble spontaneously into well-defined nanoscale morphologies, block copolymer (BCP) thin films are a versatile platform to fabricate functional nanomaterials. An important challenge to wider deployment of BCPs in nanofabrication is combining precise control over nanoscale domain orientation in BCP assemblies with scalable deposition techniques that are

applicable to large-area, curved and flexible substrates. Here, we show that spray-deposited smooth films of a nominally disordered BCP exhibit latent orientations which can be prescriptively selected by controlling solvent evaporation during spray casting. Subsequent solvent vapor annealing triggers assembly towards highly ordered cylindrical morphologies along the pathway determined by solvent evaporation in the prior spray deposition stage. Faster evaporation promotes assembly of vertically oriented cylinders spanning the entire film thickness (100-300 nm). In comparison, slow solvent evaporation permits intermicellar aggregation and incipient cylinder formation in solution, which induces horizontal cylinder assembly upon annealing. The evaporatively-controlled latent orientation mechanism presented herein elucidates how nonequilibrium phenomena during casting govern successive self-assembly pathways and facilitates a versatile method to dictate domain orientation of BCP thin films on-demand on flexible and highly curved substrates or in distinct pattern areas on the same substrate.

Nanomaterial self-assembly is a powerful platform to engineer materials from the bottom up, where the combination of component properties and mesoscale organization imbues materials with unique macroscale functionality.<sup>1-3</sup> Block copolymer (BCP) thin films serve as a canonical exemplar, wherein frustrated phase separation induces spontaneous self-assembly into ordered morphologies composed of well-defined nanoscale domains, with applications in lithographic nanopatterning<sup>4-7</sup>, nanoporous membrane synthesis<sup>8-10</sup>, nanocatalyst design<sup>11,12</sup>, and large area optical metasurface fabrication.<sup>13-15</sup> A prerequisite for BCP use in these applications is robust control over domain orientation with respect to the substrate (*i.e.*, vertical or horizontal), which is frustrated by surface energy differences between the blocks. In response, numerous strategies have

been devised to control equilibrium film energetics, including substrate functionalization<sup>16</sup>, precisely-tuned BCP chemistry<sup>17–19</sup>, designer topcoats<sup>6,20,21</sup>, surface segregating additives<sup>22,23</sup>, or plasma surface treatments.<sup>24,25</sup> Electrical<sup>26,27</sup>, magnetic<sup>28–30</sup>, and shear<sup>31–34</sup> fields can also be used to orient domains along prescribed directions. The additional steps, specialized polymers and dedicated instruments required, however, can significantly increase the cost and complexity of process scale-up and often restrict use of these methods to planar wafer substrates, presenting formidable barriers to using self-assembly in material manufacturing.

Other scalable approaches exploiting nonequilibrium self-assembly during solvent-mediated casting have also been studied as ways to control molecular organization in soft matter films.<sup>35</sup> Controlling the rate of solvent evaporation has been utilized to enhance morphological order<sup>36,37</sup> and can induce a vertical polymer concentration (or chemical potential) gradient that facilitates assembly of highly-ordered cylindrical domains with vertical orientation.<sup>38,39</sup> These solvent-mediated approaches generally utilize spin casting, which wastes a substantial amount of material, or meniscus-guided methods such as flow coating or slot die coating that are not applicable to curved surfaces. On the other hand, Osuji *et al.* have demonstrated continuous growth of nearly-dry BCP films of arbitrary thickness by electrospray deposition.<sup>40,41</sup> Spray techniques present notable advantages, as substrates with high curvature can be readily coated<sup>42</sup> and the amount of expensive wasted BCP is minimized.<sup>43</sup> Moreover, BCP films with ordered morphologies can be spray-deposited in selected areas or with designer vertical or lateral composition gradients.<sup>44</sup> Solvent evaporation is also recognized to play a role in the morphology and orientation of BCPs deposited by electrospraying,<sup>41</sup> though preserving evaporation-induced vertical domain orientation requires in situ cross-linking.<sup>45</sup>

Here, we demonstrate a scalable and programmable spray method for fabricating self-assembled, nanostructured thin films that is material-efficient, applicable to a wide variety of surfaces, and crucially, consolidates control over domain orientation and film deposition into a single step. This method rests on a mechanism in which evaporation-controlled, nonequilibrium assembly during ultrasonic spray deposition imprints the disordered, as-deposited BCP films with a latent domain orientation that fully emerges during subsequent solvent vapor annealing (SVA). Using an exemplar spray-deposited asymmetric poly(styrene-block-4-vinylpyridine) (PS-*b*-P4VP), we show that a “long” drying time ( $> \sim 140$ s) yields highly-ordered horizontal cylinders, while “short” drying times ( $< \sim 100$ s) yield highly-ordered vertical ones. This correlation is robust, and we demonstrate that orientation can be controlled by substrate temperature, forced convection, and solvent selection. In situ spectroscopic ellipsometry and grazing-incident small-angle x-ray scattering (GISAXS) characterization during film drying reveal that incipient polymer domain assembly prior to polymer vitrification is an essential precursor to well ordered, horizontally oriented cylinders during SVA. For short drying times, the rapid evaporation inhibits assembly before vitrification, yielding a more direct pathway for vertical cylinder assembly that is preferred under the selected SVA conditions. Notably, the latent horizontal orientation can be effectively erased by thermal or solvent vapor treatment, which permit short-range polymer chain rearrangement between film deposition and SVA steps.

These findings are distinguishable from prior research in which solvents and processing conditions are carefully chosen and regulated to maintain simultaneous domain assembly and vertical orientation guided by vertical solvent evaporation during casting<sup>38,46</sup>. Instead, the latent orientation mechanism effectively decouples assembly and orientation control, enabling selection between vertical and horizontal domain orientations *on-demand* at the time of film deposition

using readily adjustable parameters while maintaining short drying times (less than a few minutes). Leveraging the practical advantages of spraying, we demonstrate the versatility afforded by this on-demand orientation control to deposit and assemble cylinders with controlled orientation on flexible and highly curved surfaces, define areas with vertical and horizontal orientation on the same substrate, and create horizontal/vertical cylinder bilayer films. Beyond applications of BCP assembly, this work clarifies the outsized effect of subtle structural features in quenched BCP thin films on subsequent assembly pathways and shows how programmable ultrasonic spraying can be used to acquire deeper insights into solvent-mediated structural evolution in solution-deposited films.

## **Results and Discussion**

### **Fabrication of Block Copolymer Thin Films *via* Spray Deposition**

We adapted ultrasonic spraying, a technique that has been successfully employed for depositing large-area films of colloidal perovskite quantum dots and organic electronics,<sup>47–49</sup> to deposit smooth, well-ordered BCP thin films. In ultrasonic spraying, microscale droplets result from the breakup of liquid capillary waves generated by the transfer of mechanical energy from the nozzle vibrating at high frequency. Ultrasonic spraying has key benefits such as area-selectivity (e.g., by rastering or using masks), minimal waste, and facile application to curved surfaces. Moreover, it allows rapid film deposition with narrow droplet dispersity and requires no electrical grounding, unlike electrospraying. In the context of self-assembling BCP thin films, film nonuniformity and roughness can dramatically impact domain morphology and orientation,<sup>50</sup> yet minimizing these remains a persistent challenge for spray deposition of nanoscale films. Minimizing roughness and nonuniformity was thus the primary focus in our effort to adapt ultrasonic spraying to BCP thin films.

To emphasize the applicability of our approach to nanopatterning and related applications, we selected an asymmetric PS-*b*-P4VP diblock copolymer that has a high Flory-Huggins parameter ( $\chi$ ) enabling it to assemble P4VP cylinders with sub-20 nm domain spacings. In the spray deposition of “wet films” as done here, the effects of solution wetting, viscosity and evaporation are critical. Liquid droplets impinging on the surface must coalesce to form a continuous liquid layer, but dry fast enough to prevent dewetting or large-scale material redistribution. If evaporation is too fast, impeded droplet coalescence results in uncontrolled roughness that negatively impacts micro- and nanoscale film morphology. In the case of slow solvent evaporation on the other hand, pinning (or movement) of the solid-liquid-vapor contact line at edges of the wet film lead to the well-known coffee-ring<sup>51</sup> or mountain-like deposition patterns.<sup>52,53</sup>

We therefore selected propylene glycol monomethyl ether acetate (PGMEA) as a solvent, where its high boiling point helps to ensure film coalescence. Using the instrument described in the Methods and Supplementary Information (Figure S1), polymer concentrations above ~0.3 wt.%, were employed to increase the friction of the mobile contact line, avoiding mountain-like patterns (Figure S2). This optimization enabled us to obtain optically smooth sub-200 nm thick films (Figure 1a) at temperatures from 30 to 50 °C, though the more mottled appearance of film deposited at 50 °C indicates an increase in surface texture. Atomic force microscopy (AFM) characterization of these films (Figure 1b) confirms a low root mean squared (RMS) surface roughness of  $0.39 \pm 0.07$  nm and  $0.34 \pm 0.05$  nm for films deposited at 30 °C and 40 °C, respectively. Upon increasing the deposition temperature to 50 °C, the RMS roughness increases substantially in some small regions, reaching  $7 \pm 2$  nm in an exemplary case (Figure 1b, bottom), due to rapid solvent evaporation that produces crater-like surface texture. Raising the temperature

further increases both the roughness and nonuniformity of the film surface, so we restricted deposition temperatures used in this study to 50 °C or less.

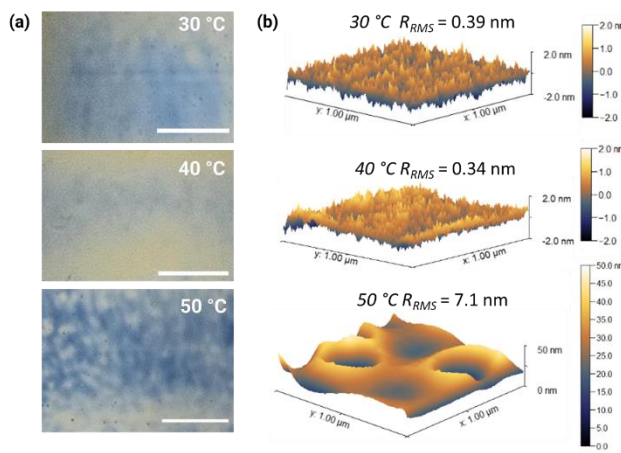


**Figure 1.** Variation of film surface uniformity with substrate deposition temperature. **(a)** Optical images of films deposited at 30 °C, 40 °C and 50 °C from top to bottom. The scale bars denote 2 mm. **(b)** AFM characterization of films deposited at 30 °C, 40 °C and 50 °C from top to bottom. Root mean squared surface roughness ( $R_{RMS}$ ) is less than 1 nm for deposition at 30 °C and 40 °C. However, the loss of droplet coalescence beginning at 50 °C results in a large increase in  $R_{RMS}$  in some regions.

### Solvent Evaporation Controlled Domain Orientation

Modulating ultrasonic deposition conditions can be used to dictate latent macromolecular structure in films (Figure 2a). Within the range of spray conditions described above, PS-*b*-P4VP thin films are deposited with an ostensible kinetically quenched disordered morphology, but with an almost imperceivable orientational bias. Highly ordered vertical or horizontal cylinder arrays emerge only after acetone SVA, with orientation depending on whether the film was spray-deposited under fast-drying or slow-drying conditions, respectively. Our substrates are functionalized by grafting a monolayer of a hydroxy-terminated poly(2-vinylpyridine) polymer (P2VP-OH) to the oxidized substrate. As we have shown previously,<sup>54</sup> this asymmetric PS-*b*-P4VP BCP assembles ordered vertical P4VP cylinders in spin- or blade-cast films with thicknesses from ~30 to over 200 nm under acetone SVA on P2VP-functionalized substrates. This can be attributed

to a surprisingly small energetic preference of P2VP for P4VP in comparison to PS and the weak preference for acetone to swell PS and P2VP over P4VP, which act synergistically to form an energetically balanced substrate interface. We emphasize that highly ordered cylinder arrays with either orientation can assemble in our sprayed films with the same P2VP substrate functionalization and acetone annealing conditions. In contrast, films sprayed on bare or PS-functionalized silicon assemble horizontal cylinders, regardless of the solvent evaporation rate during spray-deposition (Figure S3).

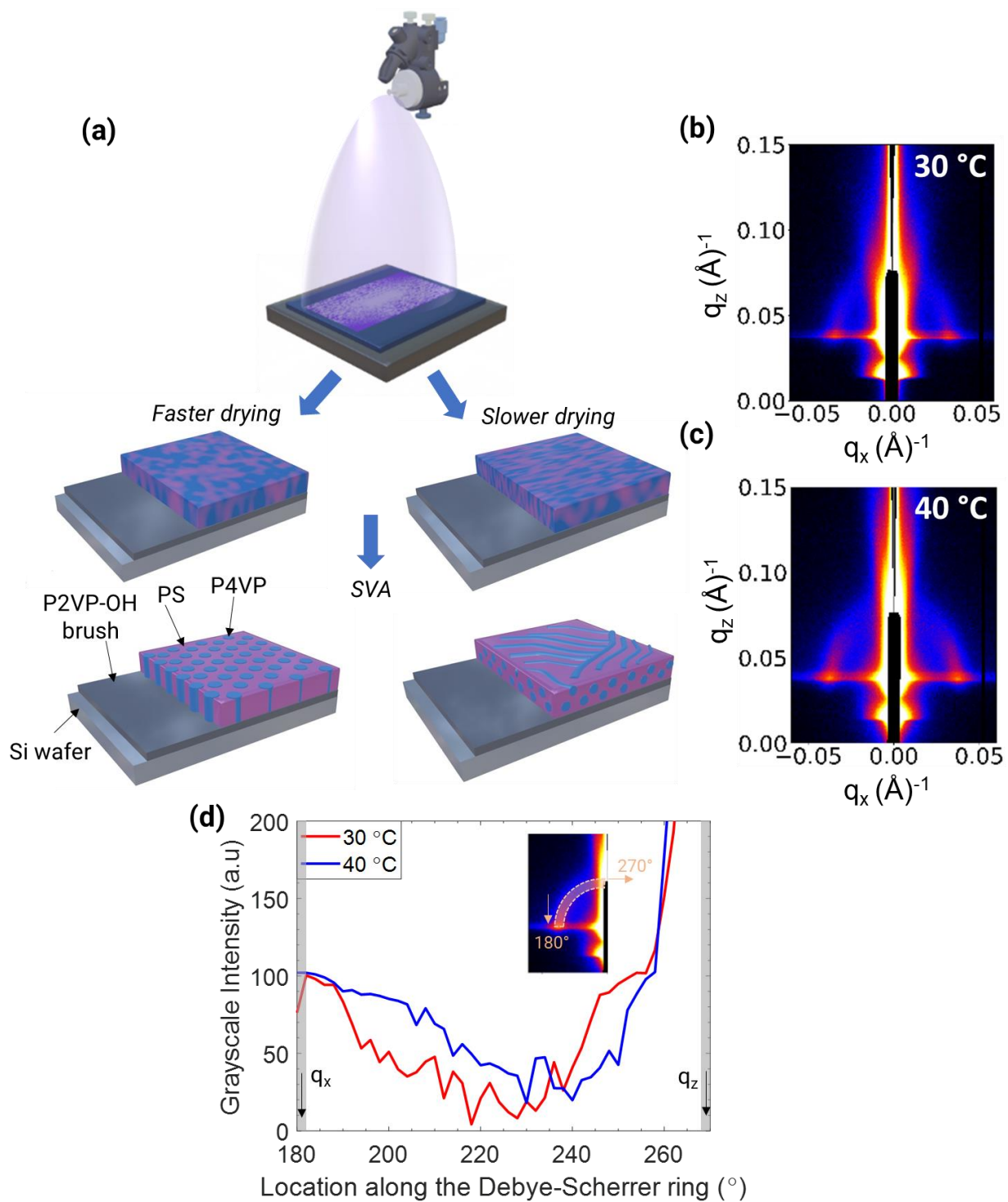


**Figure 2.** Selecting latent cylinder orientation with controlled spray deposition. (a) Illustration of the ultrasonic spray deposition and evaporation-controlled latent cylinder domain orientation. Films cast by spray deposition onto silicon substrates functionalized with a chemically grafted poly(2-vinylpyridine) monolayer brush (P2VP-OH) do not exhibit ordered cylinder domains. After solvent vapor annealing (SVA), however, films cast under fast drying conditions assemble well-ordered vertical cylinders while films cast under slow

drying conditions assemble well-ordered horizontal cylinders. GISAXS patterns acquired after spray deposition on substrates held at (b) 30 °C (slow drying) and (c) 40 °C (fast drying) indicate a poorly-ordered film, yet differences in the lateral domain spacing indicate a subtle bias in orientation for the nominally isotropic domains, as discussed in the text. (d) The difference in grayscale intensity variation along the Debye-Scherrer ring-pattern for 30 °C shown in (b) (slow drying) and 40 °C shown in (c) (fast drying) further underscore the difference in latent orientation between the samples.

We characterized the nanoscale domain morphology in PS-*b*-P4VP block copolymer films using GISAXS and electron microscopy. GISAXS patterns, provide statistically robust, large area (> 200,000  $\mu\text{m}^2$ ) characterization of domain structural features. Scanning electron microscopy (SEM) provides complementary direct visualization of the through-film cylinder structure and orientation, made possible by the inorganic replication of the P4VP domains by infiltration synthesis.<sup>55</sup> Deposition temperature has a dramatic effect on the rate of solvent evaporation, and hence film drying rate. We therefore used temperature as a primary control to assess the impact of drying on domain orientation, with longer times (several minutes) required for films to dry at 30 °C and comparatively shorter times (< ~90 s) for films deposited at 40 °C. As-deposited films do not exhibit any well-defined order, suggested by randomly meandering cylinders observed in SEM images (Supplementary Information, Figure S4a,b). GISAXS patterns of films deposited at 30 and 40 °C (Figure 2b and 2c, respectively) also exhibit weak Debye-Scherrer rings consistent with poorly ordered and isotropically oriented domains of a rapidly-quenched, microphase separated BCP.<sup>56</sup> However, the intensity along the ring in the 30 °C GISAXS pattern is enhanced near the  $q_z$  axis (Figure 2d), suggesting an inherent, if subtle, inclination toward horizontal orientation. In contrast, in the GISAXS pattern for the sample deposited at 40 °C (Figure 2c) that dried more rapidly, the intensity along the ring gradually increases as it approaches the intersection with the Yoneda band at  $q_x \approx 0.033 \text{ \AA}^{-1}$  (Figure 2d). Furthermore, the average in-plane domain spacings (measured in GISAXS from the first order peak along  $q_x$ ) decrease as a function of deposition

temperature from ~19 nm at 30 °C to ~17 nm at 50 °C (Figure S4c). Though speculative, this shift in the in-plane domain spacing can be attributed to a horizontal-to-vertical transition for the poorly-ordered cylindrical domains, as this would coincide with a reduction by a factor of  $\sqrt{3}/2$  (~19 nm to ~16.5 nm using the domain spacing at 30 °C as a reference) if assuming a hexagonal lattice. These structural difference in the as-cast films suggest a subtle bias in as-cast domain orientation, which can be controlled by deposition temperature.

After employing SVA to order the cylindrical domains, we observe a remarkable correlation between post-SVA cylinder orientation and deposition temperature. GISAXS scattering patterns acquired after SVA from a film deposited from 18  $\mu\text{L}$  of 1 % solution at 30, 40, and 50 °C are shown in Figure 3a. The pattern for deposition at 30 °C shows a vertical doublet of peaks at  $q_x \approx 0.03 \text{ \AA}^{-1}$ , arising due to reflection from the two polymer film interfaces, which corresponds to horizontal cylinders.<sup>57</sup> When the deposition temperature is increased to 40 °C, these peaks diminish in intensity while a new peak at  $q_x \approx 0.035 \text{ \AA}^{-1}$  indicative of vertically oriented cylinders emerges. At 50 °C, the vertical cylinder peak is clearly dominant while the horizontal peaks are barely visible. Top view and cross-section SEM images acquired from these samples after SVA and infiltration (Figure 3b) confirm a horizontal-to-vertical cylinder transition that occurs mainly as deposition temperature is increased from 30 to 40 °C. We note that the cylinder morphology after SVA is reasonably well ordered, as indicated by the sizes of morphological “grains” across which the hexagonal ordering motif persists. From analysis of GISAXS patterns, we estimate average grain sizes greater than 10 and 20 times the cylinder-to-cylinder distance for the horizontal and vertical orientations, respectively (see Supplementary Information, Table S1).

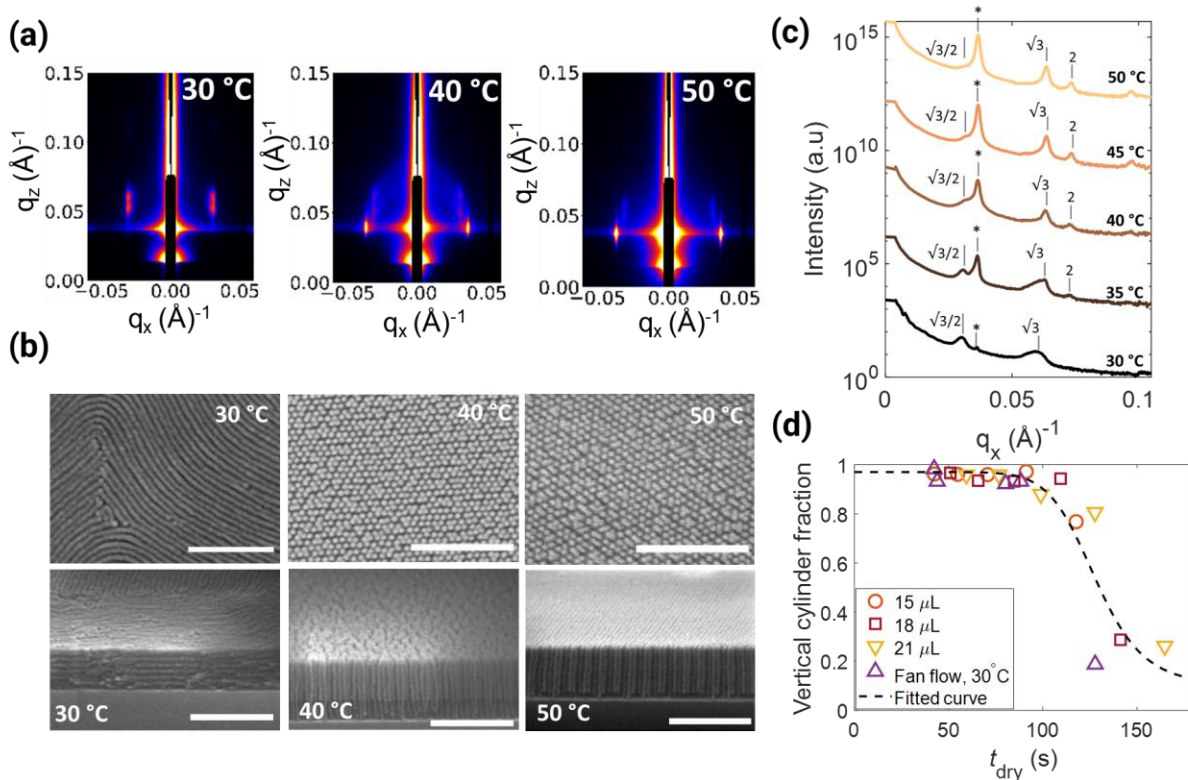


**Figure 3.** Effect of evaporation rate during casting on the self-assembled cylinder domain orientation after SVA. **(a)** Exemplar GISAXS patterns, and **(b)** top-view (top-row) and cross-sectional (bottom-row) SEM images acquired from films deposited the labelled substrate temperatures, showing an orientation change with different substrate temperatures (and hence drying rates). Selective P4VP metal oxide infiltration and oxygen plasma etching were used as a staining method for image contrast, as described in the Methods section (scale bars represent 300nm). **(c)** Line cuts along  $q_x$  from GISAXS patterns showing the evolution in domain morphology with increasing temperatures. The curves are shifted vertically for clarity. The first-order vertical orientation peak is marked by an asterisk, and the relative positions of higher-order peaks are marked by vertical lines **(d)** The fraction of vertically oriented cylinders changes as a function of film drying time during casting ( $t_{dry}$ ). Cylinder orientation fractions are estimated from GISAXS line cuts peak intensity ratios as described in the text. A transition from vertical to horizontal cylinder orientations occurs around  $t_{dry} \approx 125$  s. The dashed line is a guide to the eye.

The progressive change in cylinder orientation with increasing film deposition temperature is made clearer by analyzing the 2-dimensional GISAXS patterns using line cuts taken along  $q_x$  (Figure 3c) The first order peak for vertical cylinders ( $q_x^*$ ) occurs consistently at  $\sim 0.035 \text{\AA}^{-1}$ , whereas a peak at  $\sqrt{3}/2 q_x^*$  is present for horizontal cylinders. A higher order peak at  $\sqrt{3}q_x^*$  is expected for both cylinder orientations, while a peak at  $2q_x^*$  will only be present for vertical

cylinders as a result of hexagonal lattice symmetry. The cylinder orientation transitions from almost completely horizontal to almost completely vertical as the deposition temperature is increased from 30 °C to 50 °C, though solution concentration, volume and SVA conditions are the same across all samples.

As noted earlier, deposition temperatures directly affect solvent evaporation rate, which is known to influence domain orientation in BCP thin films.<sup>38,39</sup> However, while temperature provides a fairly robust predictor of latent cylinder orientation when other conditions are fixed, we found that horizontal orientations are in general more likely to emerge with increasing solution deposition volume (Figures S5 and S6). From this codependency, we hypothesized that latent cylinder orientation can be predicted by the time required for the wet film drying. We parameterize this drying time as  $t_{dry} = V_{dep}/R_{dry}$ , where  $V_{dep}$  is the deposition volume and  $R_{dry}$  is the volumetric rate of drying, measured separately using a video camera with  $V_{dep} = 0.1$  mL for different temperatures and concentrations (Supplementary Figure S7). We note that  $R_{dry}$  is not necessarily constant throughout the drying process, and thus the measured  $R_{dry}$  values represent a time averaged value for a 0.1 mL deposition volume. The fraction of vertical cylinders in a film can be quantified from GISAXS by the ratio of integrated intensity for vertical cylinders ( $q_x^*$ ) to the sum of integrated intensities for both  $q_x^*$  and  $\sqrt{3}/2 q_x^*$ .<sup>58,59</sup> Vertical cylinder orientation dominates when  $t_{dry} < \sim 100$  s, while horizontal cylinders dominate as  $t_{dry}$  approaches 150 s or more (Figure 2d). An approximate transition from vertical to horizontal cylinders occurs at  $t_{dry}$  equal to  $\sim 125$  s.

The drying time may be controlled by processing parameters other than temperature. As an example, we employed a fan to accelerate evaporation through forced convection (data for evaporation rate as a function of fan speed are provided in the Supplementary Information, Figure

S7b). Spraying a constant volume of a 1% PS-*b*-P4VP solution in PGMEA at a fixed temperature of 30 °C but with varying fan speeds (Figure 3d, empty violet triangles) yields a vertical-to-horizontal orientation transition with increasing  $t_{dry}$  that follows the trend observed for samples deposited without a fan at different temperatures. Similarly, drying time can be changed by selecting solvents with varying volatility. For instance, PS-*b*-P4VP films deposited without fan flow at 30 °C from blends of solutions (both 1% w/w) in toluene and PGMEA solvents exhibit a positive correlation between the vertical cylinder fraction after SVA and the toluene solvent fraction, since adding toluene accelerates film drying (Supplementary Figure S7c). Blends with a high toluene fraction (e.g., 50%), however, dry too rapidly to realize a uniform smooth film, resulting in a high fraction of horizontal cylinders after SVA due to the extreme roughness and thickness variability in these films that likely compromises the trends otherwise reported here for smooth spray-deposited films (Supplementary Figure S8). These examples (forced convection and solution blending) present alternative ways to engineer spray-deposited BCP morphology for other polymer systems or different lab or production environments.

To study the mechanism for the relationship between cylinder orientation and drying time, we characterized films *in situ* during spray deposition and subsequent film drying by both GISAXS and spectroscopic ellipsometry, as depicted schematically in Figure 4a. It is important to note that PS-*b*-P4VP micelles are already present in our PGMEA solutions at all concentrations investigated, as confirmed by dynamic light scattering (Figure S9). Linecuts were compiled from GISAXS patterns along the  $q_x$  and  $q_z$  directions in regions shown in Figure 4b, where the  $q_x$  linecut is sensitive to the population of vertically oriented structures, while the  $q_z$  linecut is sensitive to the population of horizontal ones. The scattering intensity within the linecuts along  $q_x$  and  $q_z$  for a film deposited from a 0.5% solution at a substrate temperature of 30 °C are plotted as a function

of drying time (with spray deposition at time  $\approx 0$ ) in Figures 4c and 4d, respectively, and the corresponding wet film thickness measured by ellipsometry is plotted in Figure 4e. Ordered horizontal cylinders assemble during subsequent SVA, as shown by corresponding GISAXS pattern (Figure 4e, inset).

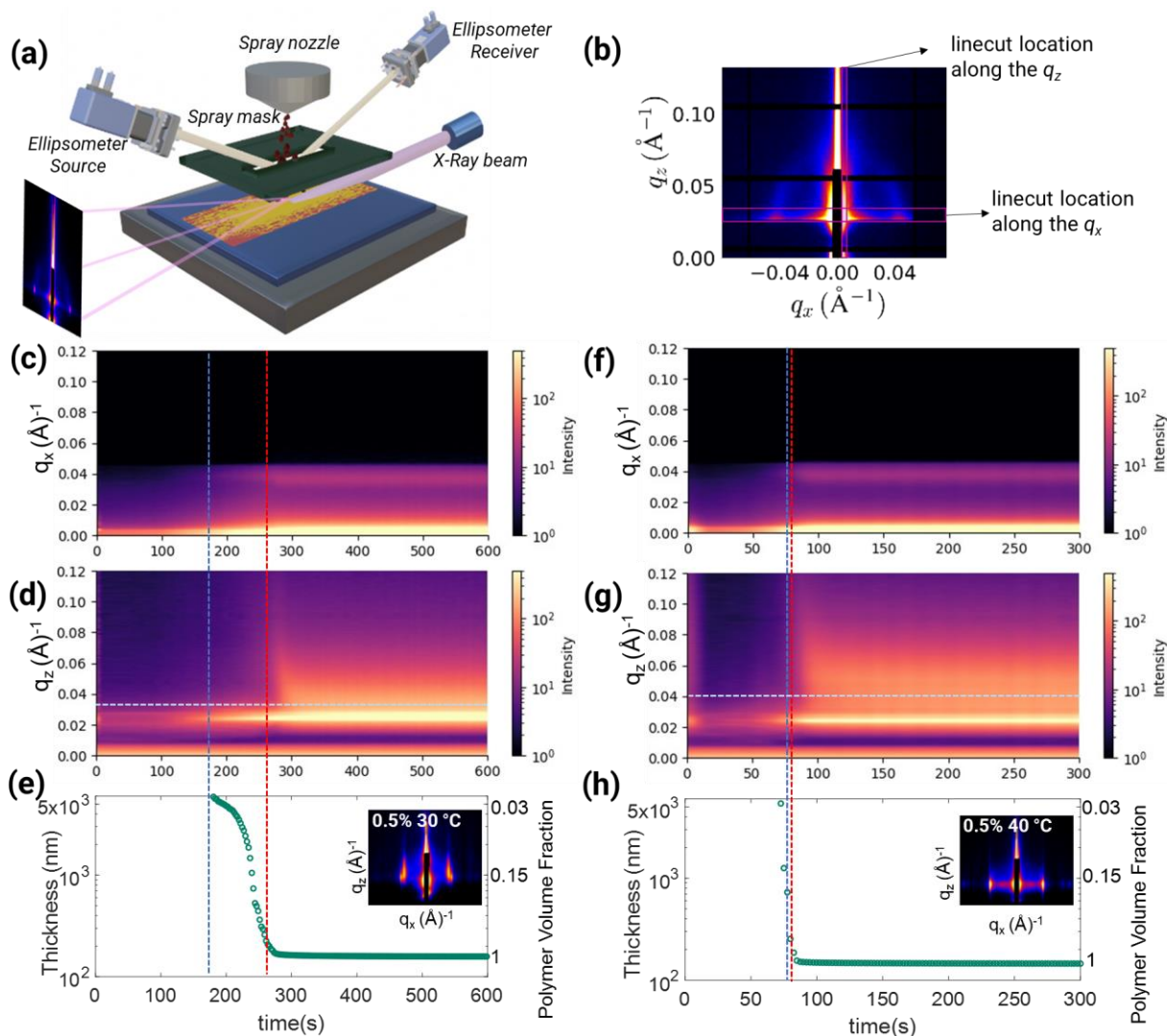


**Figure 4.** Probing nanoscale morphological evolution during spray deposition by in situ GISAXS and ellipsometry **(a)** Schematic of in situ measurement apparatus. An ultrasonic nozzle deposits polymer solution onto functionalized substrates, while GISAXS and ellipsometry characterization is performed simultaneously during deposition and liquid evaporation. A mask is used to prevent unwanted film deposition in adjacent regions of the substrates. **(b)** Exemplar GISAXS pattern showing the location of line cuts along the  $q_x$  and  $q_z$  direction used for analysis. **(c,d)** Colormaps of GISAXS intensity for a PS-*b*-P4VP film deposited from a 0.5% (w/w) solution at 30 °C are shown for the line cuts along

the **(c)**  $q_x$  and **(d)**  $q_z$  directions. **(e)** Corresponding thickness measurement by spectroscopic ellipsometry during deposition for the sample characterized in (c) and (d). Inset: GISAXS pattern for this sample after SVA. **(f,g)** Colormaps of GISAXS intensity for a PS-*b*-P4VP film deposited from a 0.5% (w/w) solution at 40 °C are shown for the line cuts along the **(f)**  $q_x$  and **(g)**  $q_z$  directions. **(h)** Corresponding thickness measurement by spectroscopic ellipsometry during deposition for the sample characterized in (f) and (g). Inset: GISAXS pattern for this sample after SVA. Thicknesses substantially greater than ~5000 nm cannot be measured reliably and accurately using this ellipsometer at a fixed angle. Dark blue and red dashed vertical lines in (c-h) represent the observed onset of cylinder self-assembly and the calculated vitrification time, respectively, as described in the text. The dashed, horizontal light blue lines in (d) and (g) denote the approximate maximums in intensity for a shoulder along the  $q_z$  direction as described in the text. We note that due to much faster drying, the full length of time in f-h is 300s, half the length of time shown for c-e, in which drying is much slower.

Two important transitions are marked by vertical lines in these plots: The red dashed line denotes the onset of film vitrification, estimated based on the wet film thickness where the substrate temperature is equal to the glass transition temperature (calculated using the Fox equation<sup>60</sup> as described in the Methods section). Meanwhile, the dark blue dashed line denotes the appearance of a scattering peak at  $q_x \approx 0.035 \text{ \AA}^{-1}$  (Figure 4c), which we attribute to incipient cylinder formation. This is corroborated by an increase in the intensity of the Yoneda band at  $q_z \approx 0.025 \text{ \AA}^{-1}$  (Figures 4d), implying the assembly of polymeric nanostructures with sufficient density for strong x-ray scattering contrast between the polymer and the solvent environment. Crucially, the gap between the onset of cylindrical formation in the wet film and vitrification is ~90 s, indicating there is ample time for cylinder self-assembly during continued evaporation. Analogous colormaps for a film deposited from the same solution at a substrate temperature of 40 °C (Figures 4f, g), along with the corresponding thickness during drying (Figure 4h), indicate a starkly different temporal sequence. The dashed vertical lines have the same meaning as before, but here they nearly overlap, indicating the cylinder domains do not form until immediately before vitrification. Vertical cylinders assemble after SVA in this case, as confirmed by GISAXS (Figure 4h, inset).

Duplicate plots of Figures 4e and 4h with a linear thickness scale are provided in Figure S10. Evaporation rates at incipient cylinder assembly are approximately 80-90 nm/s and larger than 200 nm/s for deposition at 30 °C and 40 °C, respectively.

Another key difference between scattering patterns for depositions at 30 and 40 °C is found in the presence of a broad shoulder in the scattering intensity within the linecuts along the  $q_z$  direction that appears after film vitrification. These shoulders exhibit broad intensity maxima having centers marked approximately by horizontal light blue dashed lines for the films deposited at 30 °C (Figure 4d) and 40 °C (Figure 4g), with exemplary linecuts provided in Supporting Information (Figure S11). Ascribing these peaks to incipient domain formation, their length scale is compressed in the vertical direction (i.e., shifted to higher  $q_z$ ) by ~10% for films deposited at 40 °C compared to 30 °C. This suggests that slow solvent evaporation permits more polymer rearrangement to mitigate vertical compression during casting, while fast solvent evaporation does not.

Based on the above comparisons, we infer that PS-*b*-P4VP micelles begin to pack and self-assemble into an incipient hexagonal cylinder phase long before vitrification in films cast with long drying times (e.g., at temperatures < ~35 °C), effectively imprinting the film with a latent horizontal cylinder orientation. These signs of cylinder formation appear at a surprisingly early stage — when overall solid concentrations are less than 5%. At these concentrations, intermicellar aggregation is most likely near the liquid film surface (i.e., the evaporation front) due to the locally increased polymer concentration. This may lead to the formation of proto-cylinder domains that orient horizontally to maximize contact of the lower surface energy PS with PGMEA-saturated air.

A tentative connection between the cylindrical self-assembly observed using in situ GISAXS and the empirically determined orientation transition time ( $t_{dry}$ ) can be posited by considering the

time scales for solvent diffusion ( $\tau_{diff}$ ) relative to evaporation-driven solvent transport ( $\tau_{dry}$ ). For a planar wet film,  $\tau_{dry} \sim t_{dry}$ , while  $\tau_{diff} = L_{dep}^2/D$ , where  $D$  is the solvent diffusion coefficient and  $L_{dep}$  is the deposited wet film thickness.<sup>46</sup> When  $t_{dry} < \tau_{diff}$ , solvent diffusion is slow relative to evaporation, sustaining a vertical solvent concentration gradient as the film vitrifies. In the opposite case, solvent diffusion within the film is rapid enough to minimize the formation of concentration gradients during film drying and vitrification.  $L_{dep}$  for the films presented in Figure 4 can be estimated as 30  $\mu\text{m}$  (i.e., yielding  $\sim 150$  nm films using a casting solvent with 0.5% polymer), while we estimate a magnitude of  $D$  as  $7 \times 10^{-8}$   $\text{cm}^2/\text{s}$  for PGMEA at 30  $^\circ\text{C}$  using the Stokes Einstein equation (with density = 0.96  $\text{g}/\text{cm}^3$ , molar mass = 132.16  $\text{g}/\text{mol}$ , viscosity  $\approx 0.8$  cP). These values indicate a vertical solvent concentration gradient begins to form when  $t_{dry} < \sim 128$  s. Given the high level of approximation used for this estimate, the agreement between this calculated value and transition time determined by ex situ data analysis ( $\sim 125$  s) is excellent.

Solvent evaporation during film casting is known to act as a strong driving force for domain alignment, yielding metastable vertical cylinders at the completion of film casting<sup>39,46</sup>. However, our past work has shown that SVA using acetone, a solvent that is weakly preferential for PS over P4VP, promotes robust vertical cylinder assembly in these PS-b-P4VP thin films spin- or blade-cast on P2VP-functionalized substrates across a range of film thicknesses and annealing times.<sup>54</sup> In light of this and our in situ GISAXS with synchronous ellipsometry results presented here, we posit that vertical cylinder assembly observed for fast drying films is not primarily due to alignment by solvent evaporation, but is in fact the more thermodynamically favored orientation under our SVA conditions. On the other hand, the assembly of cylinders from micelles during slow evaporation directs assembly of metastable horizontal cylinders during subsequent SVA. More specifically, we hypothesize that a steep concentration gradient under fast evaporation ( $t_{dry} <$

$\tau_{diff}$ ) inhibits polymer rearrangement during film drying. Conversely, a shallow concentration gradient under slow evaporation ( $t_{dry} > \tau_{diff}$ ) ensures that the polymer retains sufficient mobility for intermicellar packing, fusion, and an incipient stage of horizontal cylinder assembly near the free surface during film drying. These latently oriented horizontal domains can template further cylinder self-assembly,<sup>61</sup> placing the system on a pathway towards a local energy minimum featuring well-ordered horizontal cylinders. An evidently significant energy barrier impedes the energetically favored horizontal-to-vertical cylinder reorientation during SVA, even for durations of at least an hour. While surprising, similarly slow domain reorientation has been observed in thermally annealed BCPs, which can take hours to days depending on the temperature.<sup>56</sup>

We note that a vertical solvent concentration gradient (or conversely a polymer concentration gradient) promoted by solvent evaporation has been identified as a prerequisite for evaporation-induced vertical cylinder orientation during film casting in past experiments<sup>39,46</sup> and simulations.<sup>61-63</sup> Models proposed in these works generally assume that an ordered and oriented BCP phase forms from a nominally homogenous (i.e., disordered) solution at a front induced by solvent evaporation. This differs clearly from the results described here, however, in which all films are quenched with poorly ordered domains having nearly isotropic orientations. Furthermore, these models do not account for assembly pathways involving dilute pre-existing micelles as is the case here. Another practical distinction between this latent horizontal orientation mechanism and evaporative vertical alignment is the difference in time scales. For casting thin films (thickness < 1  $\mu\text{m}$ ), evaporative alignment can require casting times ranging from minutes to hours.<sup>38,39</sup> Our films dry within a few minutes, which may be compatible with high throughput processing while adding the capability to select orientations on demand with only modest process tuning. Though a separate annealing step is required, this may be optimized independently.

## **Erasure of Latent Horizontal Orientation by Intermediate Annealing**

Annealing near the  $T_g$  facilitates short-range chain relaxation and rearrangement while preventing longer range chain motion and self-assembly of the domains; for this reason, near- $T_g$  annealing has been used to remove residual stress from casting in BCP thin films.<sup>64</sup> We speculate that annealing near, but below,  $T_g$  would impart mobility for segmental relaxations necessary to remove a latent orientation, which likely requires only short range motion in the nearly isotropic domains of the as-cast films, but not sufficient mobility to enable the longer-ranged, coordinated chain motion necessary for cylinder assembly during the annealing. We therefore used thermal annealing of the BCP films prior to SVA to corroborate the metastability of the latent horizontal orientation imprinted during spray deposition. Specifically, we thermally annealed our spray deposited BCP films for 48 hours under vacuum at 90-93 °C, near the PS block glass transition temperature ( $T_g \sim 103$  °C). GISAXS pattern linecuts acquired from samples deposited at 30 and 40 °C plus SVA, with or without intermediate thermal annealing between deposition and SVA, are shown in Figure 5a. As expected, cylindrical domains are almost entirely horizontal in the sample deposited at 30 °C without thermal annealing based on the presence of a peak at  $\sqrt{3}/2 q_x^*$  and a near-absence of the  $q_x^*$  peak (bottom gray trace). In contrast, the sample deposited at 40 °C without thermal annealing exhibits predominately vertical cylinders based on the larger intensity of the  $q_x^*$  peak (top gray trace). These assessments are corroborated by top-view SEM images in Figure 5b and 5c for the samples without thermal annealing deposited at 30 and 40 °C, respectively. When thermal annealing is performed before SVA, the proportion of vertical cylinders increases regardless of deposition temperature, as evidenced by an increased relative intensity of the  $q_x^*$  peak (Figure 5a, yellow traces). A majority of cylinders are now vertical for deposition at 30 °C (bottom yellow trace), while they are nearly all vertical for deposition at 40 °C. Top view SEM images

corresponding to deposition at 30 and 40 °C (Figure 5d and 5e, respectively), reinforce this assessment. The ability to push BCP cylinders to assemble vertically by thermal annealing before SVA confirms that the ultimate orientation can be completely determined by the latent structure prescribed during deposition.

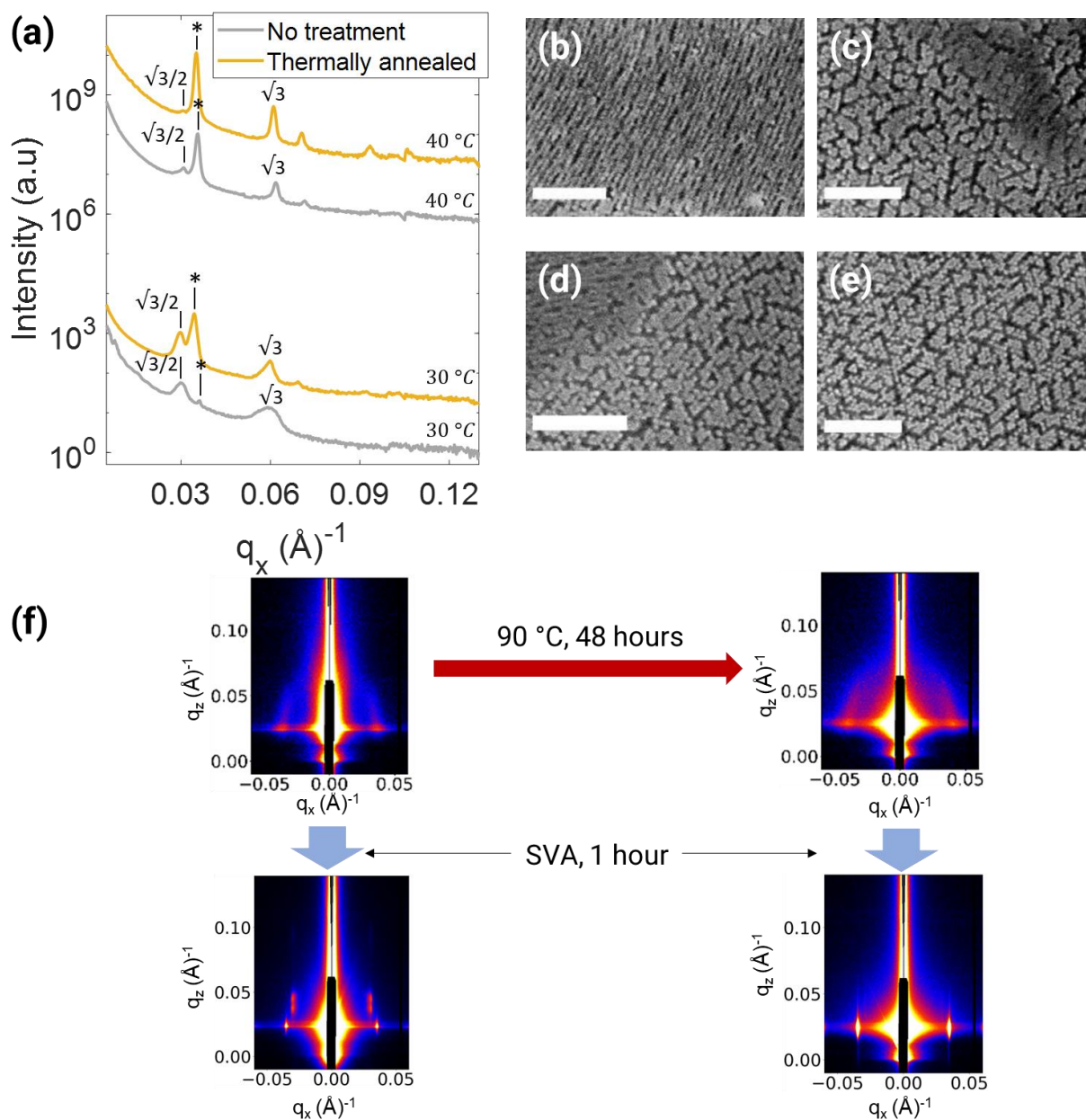


**Figure 5.** Erasure of latent horizontal cylinder orientation in as-cast films by intermediate vacuum thermal annealing at 90-93 °C for 48 hours between deposition and SVA. (a) Line

cuts along  $q_x$  from GISAXS patterns with (yellow) and without (gray) thermal annealing for samples deposited at substrate temperatures of 30 °C (bottom two curves) and 40 °C (top two curves) after SVA. The intensity growth of the primary vertical scattering peak ( $q_x^*$ , marked by an \*) and the diminishing intensity for the peak at  $\sqrt{3}/2 q_x^*$  indicate a shift towards vertical cylinder orientation is induced by thermal annealing in both cases. **(b-e)** Top view SEM images of cylinders after SVA for films deposited at **(b)** 30 °C and **(c)** 40 °C without thermal annealing, and films deposited at **(d)** 30 °C and **(e)** 40 °C with thermal annealing. Selective P4VP metal oxide infiltration was used for staining. **(f)** GISAXS patterns for PS-*b*-P4VP films deposited at 30 °C following different process pathways. Without thermal annealing, SVA induces assembly of cylinders with a mixture of vertical and horizontal orientations. A shift in scattering intensity along the Debye-Scherrer ring toward the Yoneda band after thermal annealing indicates a loss of latent horizontal orientation. After this intermediate thermal annealing, predominately vertical cylinders assemble.

Evidence for the structural changes produced by intermediate thermal annealing and its effect on the domain orientation after SVA are also apparent in representative GISAXS patterns acquired from BCP films spray-deposited at 30 °C following different processing pathways, shown in Figure 5f. As noted previously, GISAXS patterns from films deposited at this substrate temperature exhibit a higher relative intensity within the Debye-Scherrer ring near the  $q_z$  axis, which serves as a sign of latent horizontal orientation in the as-cast film (upper left pattern). As expected, these films assemble ordered cylinders with a large fraction that are horizontal after SVA (lower left pattern). Intermediate thermal annealing of the as-cast film causes the intensity within the Debye-Scherrer ring to shift toward the Yoneda band (upper right pattern), implying a loss of latent horizontal orientation, and possibly the introduction of a bias toward vertical orientation. Upon SVA, such a film yields a GISAXS pattern consistent with well-ordered vertical cylinders (lower right pattern). This result confirms our expectation that near- $T_g$  thermal annealing erases the latent horizontal domain orientation in spray-deposited films.

Annealing at even higher temperature (150 °C for 12 hours) yields similar results (Figure S12), though the tendency toward assembling vertical cylinders is less pronounced. While annealing at this temperature, above the  $T_g$  for both polymer blocks, provides more mobility for polymer chains

to relax, it can also induce further self-assembly of cylinder domains under conditions that favor horizontal cylinder orientation (i.e., high PS selectivity at the vacuum-film interface). This thermally-induced self-assembly may partially disrupt ordering during the subsequent SVA, leading to less consistent orientation, similarly to what has been shown in laser zone annealed films with shearing.<sup>31</sup> We also note that thermal annealing at 90 or 150 °C for a long duration would remove any residual casting solvent, and this removal may be responsible for the observed erasure of latent domain orientation. However, spectroscopic ellipsometry measurements show only a modest decrease in film thickness (~0.5-6%) accompanied by a minimal increase in refractive index ( $\Delta n \leq 0.02$ ) in films deposited at either 30 °C or 40 °C after thermal annealing (see Supplementary Information, Table S2), indicating that the amount of residual solvent is negligible and likely plays a marginal role in the observed latent domain orientation.

Erasure of the latent orientation may also be directly incorporated into the SVA step. In a typical SVA process for this BCP, the film is swollen with acetone vapor to ~150% of the dry film thickness. If swollen to 160% or more of the dry film thickness, however, the system undergoes an order-disorder transition<sup>54</sup> that would likely erase the latent domain orientation. We tested this by preswelling films spray deposited at 30 °C and 50°C with acetone vapor to 160% or more of the dry film thickness for 10 minutes, rapidly quenching to the dry film thickness, and then performing SVA with standard process conditions. Consistent with the thermal erasure experiments described above, the films deposited at lower temperature (slow drying) switched from horizontal to vertical orientation when the acetone preswelling step is added. The films deposited at higher temperatures (fast drying) assembled vertical cylinders in both cases (Figure S13).

## **Application of Latent Orientation Selection in Combination with Spray Deposition**

The capability to switch the latent domain orientation during ultrasonic spray deposition affords opportunities to engineer the nanostructure of self-assembled thin films on a range of surfaces with prescriptive spatial control. As an example, spraying is a facile method to coat highly-curved surfaces with minimal amounts of material, as noted previously. We demonstrated this application by coating silica lenses with  $\sim 4.7$  mm radii of curvature (Figure 6a). By simply changing the deposition temperature from 30 to 40 °C, the cylinder orientation is readily switched from horizontal to vertical as shown by representative SEM images (Figure 6b and 6c, respectively). Metal oxide nanostructures like these could be used to nanotexture small scale lenses, imparting them with highly efficient, broadband, and omnidirectional antireflectivity<sup>65</sup> for a wide range of optical sensors and devices. In addition, spraying is also possible on flexible surfaces, such as Kapton films (Supplementary Figure S14).

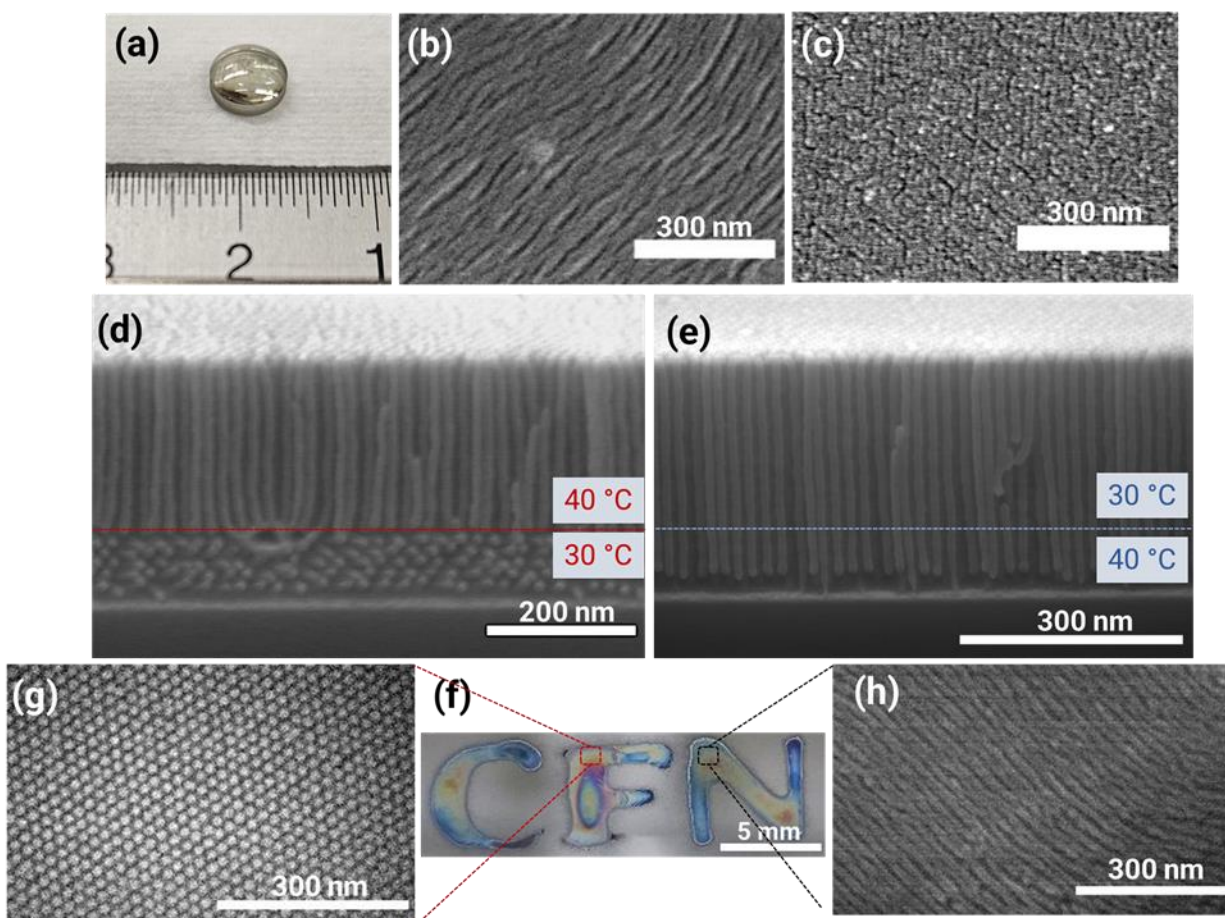


**Figure 6.** Selective cylinder orientation in spray-deposited PS-*b*-P4VP films. **(a)** Photograph of the lens with a 4.7 mm radius of curvature. **(b,c)** Top view SEM images of PS-*b*-P4VP films after SVA deposited on lenses at **(b)** 30 and **(c)** 40 °C. A ~3 nm gold film was sputtered onto the lenses for SEM imaging. **(d,e)** Cross-sectional SEM images of bilayer thin films with **(d)** a bottom layer deposited at 30 °C (horizontal cylinders) and a top layer deposited at 40 °C (vertical cylinders), and **(e)** a bottom layer deposited at 40 °C (vertical cylinders) and a top layer deposited at 30 °C. SVA is performed prior to depositing the second layer. In the latter case, vertical cylinder orientation in the top layer is templated by the bottom layer. **(f)** Sprayed “CFN” letters, where cylinders in “C” and “F” regions display vertical orientation in **(g)** and cylinders in the “N” region display horizontal orientation in **(h)**. Selective P4VP metal oxide infiltration was used for staining in all SEM images.

Spraying can also be used for sequential film deposition. In the present case, the relatively short time scales for our casting process makes it possible to cast onto previously deposited films with minimal dissolution or interdiffusion, similar to what has been demonstrated previously using blade casting<sup>66</sup>. Combining this with deterministic control of latent domain orientation enables the

formation of horizontal/vertical (bottom/top) cylinder bilayers by depositing a first layer at 30 °C and a second layer at 40 °C, as shown by SEM in Figure 6d. We note that SVA is performed for one hour after depositing each layer. Interestingly, the opposite case (vertical/horizontal bilayers) was not possible; instead, the top layer assumed the vertical orientation of the bottom layer (Figure 6e), indicating that an epitaxial relationship between layers templates the overall vertical domain orientation. Previously, Liu et al. showed that an epitaxial relationship from an underlying chemical template dominates ordering over the influence of the free surface up to a limiting thickness.<sup>67</sup> The dominance of epitaxial ordering is presumably present in the bilayer shown in Figure 6e, though it may also depend on annealing time and film thickness. This epitaxial templating may enable assembly of highly ordered vertical cylinders in uniform films with micrometer scale thickness or larger by multi-pass spray deposition. It also indicates that vertical cylinders with extremely long-range order may be directed to assemble using chemical patterns, potentially created by nonlithographic techniques<sup>68</sup>.

Finally, spraying adds a level of patternability, by rastering or masking, that is not immediately available in other nanometer film deposition methods such as spin or blade coating. We demonstrate this here using masks to deposit distinct regions with vertical or cylinder domain orientation on the same substrate and using the same BCP and annealing treatment (Figure 6f-6h). In line with our prior results, films deposited at 40 °C in the “C” and “F” regions assemble vertical cylinders after SVA (Figure 6g), while the film deposited at 30 °C in the “N” region assembles horizontal cylinders (Figure 6h). Some film thickness variation is observed primarily due to distribution of deposition material in the spray plume.

Importantly, the spray deposition process demonstrated here is rapid, with deposition occurring within seconds and drying within a few minutes or less. By spraying on a moving sample, larger

areas with high uniformity can readily be deposited (Figure S15). Moreover, while films presented here were typically annealed for one hour, well-ordered vertical or horizontal cylinder domains were also obtained using a rapid SVA step completed in only 5 min (Figure S16). Advances in zone<sup>69</sup> and immersion<sup>70</sup> annealing methods make it possible to envision spray coating as an integral component in continuous roll-to-roll manufacturing processes that leverage self-assembly. Moreover, globally aligned horizontal cylinders may be assembled using unidirectional shear before SVA.<sup>31</sup>

While the above examples demonstrate the advantages of on-demand orientation selection for a specific spray-deposited PS-*b*-P4VP BCP, the accompanying insights about latent domain orientation are generalizable to other systems. For example, we observe a similar dependence of the orientation of P4VP cylinders (using the same PS-*b*-P4VP BCP) that are blade-cast from PGMEA or toluene, two solvents with comparable selectivities for PS over P4VP, but which dry on the time scale of minutes (> 7) or seconds (< 45), respectively (Figure S17). Orientation selection can also be implemented in the spray deposition of distinct, but analogous, self-assembling BCPs. To demonstrate this, we spray-deposited films of an asymmetric poly(styrene-block-methyl methacrylate) (PS-*b*-PMMA) BCP with a majority PMMA block that assembled PS cylinders. In emulation of the PS-*b*-P4VP/PGMEA system, the PS-*b*-PMMA BCP was dissolved in anisole, a nonvolatile solvent selective for the PMMA majority block, and ~140 nm thick films were deposited on a substrate functionalized with a PS-*r*-PMMA random copolymer (45% PS) that partly balances interfacial energies between the blocks.<sup>71</sup> After thermal annealing for 5 minutes at 270 °C, films deposited on substrates held at 25 °C assemble horizontal cylinders (slow drying), while films deposited at 60 °C (rapid drying) assembled vertical cylinders (Figure S18).

These results further support the proposed latent domain orientation mechanism and indicate how it may be applied to other BCPs.

## Conclusions

In summary, we have identified the presence of a latent domain orientation in cylinder-assembling BCP thin films which depends on the rate of solvent evaporation during casting and determines subsequent assembly pathways. By controlling evaporation rate in spray deposition, we have realized prescriptive, on-demand selection of vertical or horizontal BCP cylinder orientation, adding a key element to the “toolbox” for scalable material engineering by self-assembly. The combination with spraying affords further advantages of material economy, substrate flexibility (e.g., for curved or irregular surfaces), and orientational patterning. Our results yield deeper insights into the complex, pathway-dependent self-assembly that occurs in BCP films. Ultimately, however, the ability to control structural orientation at the nanoscale by regulating deposition parameters extends beyond block copolymers, holding important implications for the scalable production of functional polymer, perovskite, nanoparticle, and nanocomposite films.

## Methods

**Materials and Substrate Preparation.** Hydroxyl-terminated P2VP “brush” (P2VP-OH, number of average molar mass  $M_n = 6.3$  kg/mol, and polydispersity index of  $PDI = 1.06$ ), cylinder-forming PS-*b*-P4VP diblock copolymer ( $M_n = 19$ -*b*-5 kg/mol;  $PDI = 1.06$ ), and cylinder-forming PS-*b*-PMMA diblock copolymer ( $M_n = 20$ -*b*-51 kg/mol;  $PDI = 1.06$ ) were purchased from Polymer Source and used as received. A hydroxy-terminated PS-*r*-PMMA-OH random copolymer with 45 mol % PS was obtained from Dow Chemical as a solution in PGMEA and diluted to 1% (w/w).

Silicon substrates used for the experiments were boron-doped polished Si wafers, 500  $\mu\text{m}$  thick,  $\langle 100 \rangle$  orientation, with a resistivity range of 0–100 ohm-cm (University Wafers). Propylene glycol monomethyl ether acetate (PGMEA), 2-methoxyethanol, anisole and toluene were purchased from Sigma-Aldrich and used without further purification. Fused silica lenses were purchased from Edmund Optics (model 45-077, effective focal length = 6 mm, radius of curvature = 4.7 mm).

Silicon wafers were cut and treated with  $\text{O}_2$ -plasma (Nordson March CS-1701 RIE) for 120 s at 21 W to clean the surface of organic contaminants. A film of the P2VP-OH was spun onto Si wafer at 1500 rpm for 30s from a 1% (w/w) solution in PGMEA. The coated wafers were then baked on a hot plate (Apogee Bake Plate) at 250  $^\circ\text{C}$  for 5 min under continuous nitrogen purging to graft the brush onto the substrate. Ungrafted brush was removed by rinsing with neat PGMEA on a spin coater at 3000 rpm for 30s. The same method was used for PS-*r*-PMMA-OH. For depositions on curved surfaces, a similar recipe is applied onto the lenses, with the only difference being that a 3% (w/w) P2VP-OH solution of in PGMEA was used to ensure a film thick enough for efficient grafting across the lens.

Blade-coated PS-*b*-P4VP films were cast using a home-built blade coater from either a toluene (2% w/w) or a PGMEA solution (1% w/w), yielding films 140-160 nm and 160-180 nm thick, respectively. The toluene solution volume was 25  $\mu\text{L}$  and the blade-substrate gap was  $\sim 50$   $\mu\text{m}$ . The PGMEA solution volume was 50  $\mu\text{L}$  and the blade-substrate gap was  $\sim 40$   $\mu\text{m}$ . A stage velocity of 70 mm/s was used in both cases. Samples were annealed by SVA as described below for 30 or 60 minutes.

**Thin Film Fabrication by Ultrasonic Spray Deposition.** PS-*b*-P4VP diblock copolymer films were deposited onto functionalized Si wafers via a Python programmable ultrasonic spray

apparatus shown in the Supplementary Information (Figure S1). Substrates were placed on an Instec TC104 hot plate connected to an mK2000B controller, held at temperatures from 25 to 60 °C. Programmable, motorized vertical and horizontal stages control the nozzle-substrate distance and the sample position, respectively. Liquid atomization and spray plume generation were achieved using a Sono-Tek ALIGN model with an Impact spray shaping assembly. A mask with a 5 mm wide slit was used to define the deposition area and prevent contamination of other regions of the substrate. Under typical spray conditions, a power of 1 W was supplied to the ultrasonic nozzle, held 45 mm above the deposition substrate. Dry nitrogen carrier gas used to direct droplets toward the substrate was supplied at 6 L/min with an upstream pressure of 20 psig as controlled by a regulator. The droplet size generated by ultrasonic generator can be estimated empirically based on the Kelvin equation<sup>72</sup> for the wavelength of the sonically generated capillary waves as,

$$D_{0.5} = 0.34 \left( \frac{8\pi\sigma}{\rho f^2} \right)^{1/3} \quad (1)$$

in which  $D_{0.5}$ ,  $\sigma$ ,  $\rho$ , and  $f$  represents the mean droplet diameter, liquid surface tension, density of the liquid and frequency of the droplet generator. Using Eq.1, we estimated the mean droplet diameter of 12  $\mu\text{m}$  for the frequency used in our experiments (120 kHz).

Polymer solutions were delivered to the nozzle from 10 ml luer lock syringes (BD) using multiple New Era syringe pumps (NE-1000) through 1/8 in. OD, 1/16 in. ID PTFE tubing to control polymer concentration and composition. Ultrasonic excitation was triggered using a 5 V TTL from an Arduino circuit. Solution concentration was controlled by mixing pure solvent with 1% (w/w) polymer solutions in prescribed ratios using separate syringe pumps with transfer tubes merging at a Y-connector (Idex natural PEEK, 0.020" Bore, 1/8" OD Tubing) prior to the spray nozzle. Typical solution flow rates and volumes were 0.3 mL/min. and 15-24  $\mu\text{L}$ , respectively,

yielding films from 100–200 nm thick, as measured by spectral reflectance (Filmetrics, F-20 UV). Liquid flow rate, substrate temperature and stage motion were controlled by a Python script. For the added convective air flow, a fan (Noctua, NF-A8 PWM) with a 12V controller (NA-FC1) was placed near the deposition surface.

After the deposition, automated SVA in acetone vapor was performed as described previously.<sup>54</sup> Swollen film thicknesses during SVA were maintained at a value of  $\sim 1.4$ - $1.55\times$  the dry film thickness for durations of 3-60 minutes. Films swollen to ratios less than  $1.4\times$  the dry thickness do not have the mobility to assemble well-ordered cylinders, while the system undergoes an order-disorder transition if swollen with acetone to a ratio of 1.6 or more.<sup>54</sup> Exposure to a controlled acetone atmosphere by SVA plasticizes the deposited polymer thin film, providing mobility for assembly of an ordered hexagonal cylinder morphology. Importantly, acetone exhibits only modest selectivity for swelling PS over P4VP; as a result, acetone SVA on this P2VP-functionalized substrates promotes robust vertical cylinder orientation across a broad thickness range. A vacuum oven (VWR-symphony 414004-580) was used to thermally anneal selected samples at preset temperatures of 90 °C and 150 °C for 48 and 12 hours, respectively. PS-*b*-PMMA thin films were annealed on a hot plate (Apogee Bake Plate) at 270 °C for 5 min under continuous nitrogen purging.

**SEM Imaging.** Thin film surface morphologies were characterized using a Hitachi S-4800 Scanning Electron Microscope (SEM) with 10 kV accelerating voltage. To provide domain contrast for electron microscopy, Alumina and Zinc Oxide (AZO) microdosing vapor phase infiltration was performed at 85 °C with diethyl zinc (DEZ) and trimethylaluminum (TMA) as metal-organic precursors and with water vapor as an oxidant using a commercial atomic layer deposition tool (Cambridge Ultratech Savannah S100) with a base pressure  $< 1$  torr as described

elsewhere.<sup>55,66</sup> Alternatively, indium oxide vapor phase infiltration conducted in a Veeco Savannah S200 and using 4 cycles of 60 s of precursor exposure and 60 s of nitrogen purging at 85 °C yielded similar quality domain contrast.<sup>55</sup> Inorganic replicas of the self-assembled structure were revealed by oxygen plasma ashing (March Plasma CS1701F) for 40 s at 20W and a pressure of 100 mTorr.

**Grazing-Incidence Small-Angle X-ray Scattering (GISAXS).** The 11-BM Complex Materials Scattering (CMS) beamline at the National Synchrotron Light Source II (NSLS-II) was used to acquire in situ and ex situ GISAXS measurements. A photon-counting area detector (Dectris Pilatus 2 M) was placed at a location of 5.05 m from the sample to collect two-dimensional scattering images. Samples were measured using an X-ray beam of 13.5 keV ( $\lambda = 0.09184$  nm). The x-ray beam width was approximately 200  $\mu\text{m}$  and a 10 s integration time at incidence angles of 0.05°, 0.08°, 0.10°, 0.12°, and 0.15° was used for the ex-situ sample measurements. For in situ measurements, the GISAXS spot, spray plume, and ellipsometry light spot were co-aligned, enabling simultaneous film deposition, GISAXS and ellipsometry measurement at the same location. A 5 s integration time at an incidence angle of 0.10° was employed and data was collected every ~6 s. Scattering patterns were acquired after sample drying at two incidence angles in two adjacent areas are taken to confirm that x-ray beam damage did not substantially alter the final GISAXS patterns. Silver behenate (AgBH) powder was used as a standard for data conversion to  $q$ -space. Data analyses on experimental X-ray scattering detector images were performed using the SciAnalysis software package [<https://github.com/CFN-softbio/SciAnalysis>].

Morphology information was retrieved by taking a line cut along the in-plane direction ( $q_x$ , scattering vector in normal to the plane-of-incidence direction) at  $q_z = 0.025 \text{ \AA}^{-1}$  with an integration window of  $0.005 \text{ \AA}^{-1}$ . For in situ data, line cuts along the  $q_z$  direction were acquired at

$q_x = 0.0055 \text{ \AA}^{-1}$  with an integration window of  $0.002 \text{ \AA}^{-1}$ . The peak center position and integrated peak intensity were calculated using a Gaussian fitting function with a linear background using Matlab or SciAnalysis. Debye-Scherrer ring signal intensity analysis was performed using the ImageJ Oval Profile plugin. GISAXS patterns were first converted to 16-bit greyscale images, and pixel values are calculated with 180 data points along the circumference of the Debye-Scherrer ring.

**Ellipsometry Measurements.** Spectroscopic ellipsometry was performed using a M-2000 (J. A. Woollam) at a fixed angle of incidence of  $65^\circ$  in the wavelength range of  $370 \text{ nm} < \lambda < 1600 \text{ nm}$  and a focused spot size of approximately  $0.7 \text{ mm} \times 1.5 \text{ mm}$ . For concurrent in situ GISAXS and thickness measurements, the GISAXS beam was below the mask while the ellipsometry beam and its reflection passed through the mask slit, with ellipsometric data collected every  $\sim 2.5 \text{ s}$ . The data were fitted to a three-layer model consisting of silicon substrate, a  $1 \text{ nm}$  native oxide layer and the polymer film. The polymer film layer was modeled using the Cauchy dispersion equation,  $n(\lambda) = A + \frac{B}{\lambda^2} + \frac{C}{\lambda^4}$  and  $k(\lambda) = 0$ , where  $n$  is the refractive index,  $\lambda$  is the wavelength of light and  $k$  is the absorption coefficient.  $A$ ,  $B$ ,  $C$ , film thickness, and surface roughness are the adjustable fit parameters. To ensure the fit parameters correspond to physically realistic values,  $A$  was restricted to values between 1.3 and 1.6, while  $B$  and  $C$  were restricted to positive numbers. Before each measurement, signal intensity is maximized by alignment of detector, and data in the wavelength range of  $400\text{-}800 \text{ nm}$  were used for dynamic fitting. The typical mean squared error was  $< 10$ .

**Vitrification Time Calculation.** The time for the onset of film vitrification (red dashed lines in Figure 4c-4h), were estimated using the Fox equation by setting the system glass transition temperature ( $T_g$ ) to the deposition temperature ( $T_d$ ), resulting in

$$\frac{1}{T_d} = \frac{w_P}{T_{g,PS}} + \frac{(1-w_P)}{T_{m,PGMEA}}$$

where  $T_{g,PS}$  and  $T_{m,PGMEA}$  are the PS glass transition temperature (378.15 K<sup>22</sup>) and the PGMEA melting temperature (206.15 K), respectively. This equation was used to solve for the polymer weight fractions ( $w_P$ ) at vitrification, which was then converted to volume fractions using known PGMEA and PS densities. From the final “dry” film thicknesses and these volume fractions, the wet film thickness at vitrification can be calculated. Finally, the corresponding time for the vitrification onset was estimated from the in situ ellipsometry measurements. Estimated times for the onset of vitrification are 263 s and 82 s for the depositions at 30 °C and 40 °C, respectively.

## ASSOCIATED CONTENT

### Supporting Information.

The following files are available free of charge.

In-situ spray-deposition tool and schematic shown in Fig. S1, “mountain-like” deposition patterns observed with lower concentrations of PS-*b*-P4VP shown in Fig. S2, GISAXS patterns of substrate functionalization and deposition temperature on the morphology of deposited PS-*b*-P4VP cylinders in Fig. S3, scanning electron microscopy images and lateral domain spacings as a function of deposition temperature shown in Fig. S4, horizontal linecuts from GISAXS patterns from samples deposited at different temperatures shown in Fig. S5, estimated vertical cylinder fraction as a function of deposition temperature are shown in Fig. S6, measured drying rates are shown in Fig. S7, horizontal GISAXS linecut plots and GISAXS patterns for different toluene fractions are shown in Fig. S8, dynamic light scattering measurement of PS-*b*-P4VP solutions are shown in Fig. S9, linear scale plots of film thickness measured by in situ ellipsometry are shown

in Fig. S10, exemplary linecuts through the broad shoulder in scattering intensity along the  $q_z$  direction referred to in Figure 4d and g are shown in Fig. S11, GISAXS characterization of the effects of intermediate thermal annealing are shown in Fig. S12, top-view SEM images for the erasure of latent domain orientation using the controlled swelling ratio with acetone are shown in Fig. S13, optical and top-view SEM images for depositions on flexible Kapton film are shown in Fig. S14, optical images and top and cross-sectional view of a rastered deposition are shown in Fig. S15, GISAXS linecut plots of self-assembled film within 5 minutes of SVA and corresponding SEM images are shown in Fig. S16, top-view SEM images for latent orientation in PS-*b*-P4VP block copolymer films blade cast from PGMEA or toluene is shown in Fig. S17, top-view SEM images for PS cylinder assembling PS-*b*-PMMA films after thermal annealing spray deposited from anisole solution at different deposition temperatures are shown in Fig. S18, average grain size for the hexagonal cylinder morphologies by Scherrer analysis of GISAXS patterns are shown in Table S1, and measured film thickness and refractive indices (at 632.8 nm wavelength) of PS-*b*-P4VP films after deposition, thermal treatment and SVA using ex situ spectroscopic ellipsometry are shown in Table S2.

## AUTHOR INFORMATION

### Corresponding Authors

\*[gdoerk@bnl.gov](mailto:gdoerk@bnl.gov)

### Author Contributions

Experimental studies including instrumentation design, sample preparation, imaging, in situ deposition and GISAXS/ellipsometry were performed by S.C., B.B. and G.S.D.; data analysis was performed S.C., and G.S.D.; AFM measurements were performed by S.C., and D.N.; results were

interpreted by G.S.D., S.C., R.L., E.T., and B.B. All authors have contributed to reviewing and editing the manuscript and approve the published version.

## ACKNOWLEDGMENT

This research used the Materials Synthesis and Characterization facility and the X-ray scattering partner user program at the Center for Functional Nanomaterials (CFN) and the 11-BM end station of the National Synchrotron Light Source II (NSLS-II), which are U.S. Department of Energy (DOE) Office of Science User Facilities, at Brookhaven National Laboratory under Contract No. DE-SC0012704. S.C., B.B., and G.S.D. were supported by a DOE Early Career Research Program grant. G.S.D. thanks K. Yager for suggestions to improve this manuscript.

## REFERENCES

- (1) Appel, E. A.; Tibbitt, M. W.; Webber, M. J.; Mattix, B. A.; Veisheh, O.; Langer, R. Self-Assembled Hydrogels Utilizing Polymer–Nanoparticle Interactions. *Nat. Commun.* **2015**, *6* (1), 6295. <https://doi.org/10.1038/ncomms7295>.
- (2) Vatankhah-Varnosfaderani, M.; Keith, A. N.; Cong, Y.; Liang, H.; Rosenthal, M.; Sztucki, M.; Clair, C.; Magonov, S.; Ivanov, D. A.; Dobrynin, A. V.; Sheiko, S. S. Chameleon-like Elastomers with Molecularly Encoded Strain-Adaptive Stiffening and Coloration. *Science* **2018**, *359* (6383), 1509–1513. <https://doi.org/10.1126/science.aar5308>.
- (3) Santos, P. J.; Gabrys, P. A.; Zornberg, L. Z.; Lee, M. S.; Macfarlane, R. J. Macroscopic Materials Assembled from Nanoparticle Superlattices. *Nature* **2021**, *591* (7851), 586–591. <https://doi.org/10.1038/s41586-021-03355-z>.
- (4) Park, M.; Harrison, C.; Chaikin, P. M.; Register, R. A.; Adamson, D. H. Block Copolymer Lithography: Periodic Arrays of ~1011 Holes in 1 Square Centimeter. *Science* **1997**, *276* (5317), 1401–1404. <https://doi.org/10.1126/science.276.5317.1401>.
- (5) Ruiz, R.; Kang, H.; Detcheverry, F. A.; Dobisz, E.; Kercher, D. S.; Albrecht, T. R.; de Pablo, J. J.; Nealey, P. F. Density Multiplication and Improved Lithography by Directed Block Copolymer Assembly. *Science* **2008**, *321* (5891), 936–939. <https://doi.org/10.1126/science.1157626>.
- (6) Suh, H. S.; Kim, D. H.; Moni, P.; Xiong, S.; Ocola, L. E.; Zaluzec, N. J.; Gleason, K. K.; Nealey, P. F. Sub-10-Nm Patterning via Directed Self-Assembly of Block Copolymer Films with a Vapour-Phase Deposited Topcoat. *Nat. Nanotechnol.* **2017**, *12* (6), 575–581. <https://doi.org/10.1038/nnano.2017.34>.
- (7) Tsai, H.; Pitera, J. W.; Miyazoe, H.; Bangsaruntip, S.; Engelmann, S. U.; Liu, C.-C.; Cheng, J. Y.; Bucchignano, J. J.; Klaus, D. P.; Joseph, E. A.; Sanders, D. P.; Colburn, M. E.; Guillorn, M. A. Two-Dimensional Pattern Formation Using Graphoepitaxy of PS-b-PMMA Block

- Copolymers for Advanced FinFET Device and Circuit Fabrication. *ACS Nano* **2014**, *8* (5), 5227–5232. <https://doi.org/10.1021/nn501300b>.
- (8) Ahn, H.; Park, S.; Kim, S.-W.; Yoo, P. J.; Ryu, D. Y.; Russell, T. P. Nanoporous Block Copolymer Membranes for Ultrafiltration: A Simple Approach to Size Tunability. *ACS Nano* **2014**, *8* (11), 11745–11752. <https://doi.org/10.1021/nn505234v>.
  - (9) Hampu, N.; Werber, J. R.; Chan, W. Y.; Feinberg, E. C.; Hillmyer, M. A. Next-Generation Ultrafiltration Membranes Enabled by Block Polymers. *ACS Nano* **2020**, *14* (12), 16446–16471. <https://doi.org/10.1021/acsnano.0c07883>.
  - (10) Feng, X.; Tousley, M. E.; Cowan, M. G.; Wiesenauer, B. R.; Nejati, S.; Choo, Y.; Noble, R. D.; Elimelech, M.; Gin, D. L.; Osuji, C. O. Scalable Fabrication of Polymer Membranes with Vertically Aligned 1 Nm Pores by Magnetic Field Directed Self-Assembly. *ACS Nano* **2014**, *8* (12), 11977–11986. <https://doi.org/10.1021/nn505037b>.
  - (11) Huang, L.; Chen, P.-C.; Liu, M.; Fu, X.; Gordiichuk, P.; Yu, Y.; Wolverton, C.; Kang, Y.; Mirkin, C. A. Catalyst Design by Scanning Probe Block Copolymer Lithography. *Proc. Natl. Acad. Sci.* **2018**, *115* (15), 3764–3769. <https://doi.org/10.1073/pnas.1800884115>.
  - (12) Choi, Y.; Cha, S. K.; Ha, H.; Lee, S.; Seo, H. K.; Lee, J. Y.; Kim, H. Y.; Kim, S. O.; Jung, W. Unravelling Inherent Electrocatalysis of Mixed-Conducting Oxide Activated by Metal Nanoparticle for Fuel Cell Electrodes. *Nat. Nanotechnol.* **2019**, *14* (3), 245–251. <https://doi.org/10.1038/s41565-019-0367-4>.
  - (13) Alvarez-Fernandez, A.; Cummins, C.; Saba, M.; Steiner, U.; Fleury, G.; Ponsinet, V.; Guldin, S. Block Copolymer Directed Metamaterials and Metasurfaces for Novel Optical Devices. *Adv. Opt. Mater.* **2021**, *9* (16), 2100175. <https://doi.org/10.1002/adom.202100175>.
  - (14) Kulkarni, A. A.; Doerk, G. S. Hierarchical, Self-Assembled Metasurfaces via Exposure-Controlled Reflow of Block Copolymer-Derived Nanopatterns. *ACS Appl. Mater. Interfaces* **2022**, *14* (23), 27466–27475. <https://doi.org/10.1021/acsnano.2c05911>.
  - (15) Kim, J. Y.; Kim, H.; Kim, B. H.; Chang, T.; Lim, J.; Jin, H. M.; Mun, J. H.; Choi, Y. J.; Chung, K.; Shin, J.; Fan, S.; Kim, S. O. Highly Tunable Refractive Index Visible-Light Metasurface from Block Copolymer Self-Assembly. *Nat. Commun.* **2016**, *7* (1), 12911. <https://doi.org/10.1038/ncomms12911>.
  - (16) She, M.-S.; Lo, T.-Y.; Ho, R.-M. Long-Range Ordering of Block Copolymer Cylinders Driven by Combining Thermal Annealing and Substrate Functionalization. *ACS Nano* **2013**, *7* (3), 2000–2011. <https://doi.org/10.1021/nn305725q>.
  - (17) Zhang, R.; Qiang, Z.; Wang, M. Integration of Polymer Synthesis and Self-Assembly for Controlled Periodicity and Photonic Properties. *Adv. Funct. Mater.* **2021**, *31* (1), 2005819. <https://doi.org/10.1002/adfm.202005819>.
  - (18) Liang, R.; Xue, Y.; Fu, X.; Le, A. N.; Song, Q.; Qiang, Y.; Xie, Q.; Dong, R.; Sun, Z.; Osuji, C. O.; Johnson, J. A.; Li, W.; Zhong, M. Hierarchically Engineered Nanostructures from Compositionally Anisotropic Molecular Building Blocks. *Nat. Mater.* **2022**, *21* (12), 1434–1440. <https://doi.org/10.1038/s41563-022-01393-0>.
  - (19) Sun, Z.; Liu, R.; Su, T.; Huang, H.; Kawamoto, K.; Liang, R.; Liu, B.; Zhong, M.; Alexander-Katz, A.; Ross, C. A.; Johnson, J. A. Emergence of Layered Nanoscale Mesh Networks through Intrinsic Molecular Confinement Self-Assembly. *Nat. Nanotechnol.* **2023**, *18* (3), 273–280. <https://doi.org/10.1038/s41565-022-01293-z>.
  - (20) Bates, C. M.; Seshimo, T.; Maher, M. J.; Durand, W. J.; Cushen, J. D.; Dean, L. M.; Blachut, G.; Ellison, C. J.; Willson, C. G. Polarity-Switching Top Coats Enable Orientation of Sub-

- 10-Nm Block Copolymer Domains. *Science* **2012**, *338* (6108), 775–779. <https://doi.org/10.1126/science.1226046>.
- (21) Kim, E.; Kim, W.; Lee, K. H.; Ross, C. A.; Son, J. G. A Top Coat with Solvent Annealing Enables Perpendicular Orientation of Sub-10 Nm Microdomains in Si-Containing Block Copolymer Thin Films. *Adv. Funct. Mater.* **2014**, *24* (44), 6981–6988. <https://doi.org/10.1002/adfm.201401678>.
- (22) Doerk, G. S.; Yager, K. G. Rapid Ordering in “Wet Brush” Block Copolymer/Homopolymer Ternary Blends. *ACS Nano* **2017**, *11* (12), 12326–12336. <https://doi.org/10.1021/acsnano.7b06154>.
- (23) Doerk, G. S.; Li, R.; Fukuto, M.; Yager, K. G. Wet Brush Homopolymers as “Smart Solvents” for Rapid, Large Period Block Copolymer Thin Film Self-Assembly. *Macromolecules* **2020**, *53* (3), 1098–1113. <https://doi.org/10.1021/acs.macromol.9b02296>.
- (24) Oh, J.; Suh, H. S.; Ko, Y.; Nah, Y.; Lee, J.-C.; Yeom, B.; Char, K.; Ross, C. A.; Son, J. G. Universal Perpendicular Orientation of Block Copolymer Microdomains Using a Filtered Plasma. *Nat. Commun.* **2019**, *10* (1), 2912. <https://doi.org/10.1038/s41467-019-10907-5>.
- (25) Oh, J.; Shin, M.; Kim, I. S.; Suh, H. S.; Kim, Y.; Kim, J. K.; Bang, J.; Yeom, B.; Son, J. G. Shear-Rolling Process for Unidirectionally and Perpendicularly Oriented Sub-10-Nm Block Copolymer Patterns on the 4 in Scale. *ACS Nano* **2021**, *15* (5), 8549–8558. <https://doi.org/10.1021/acsnano.1c00358>.
- (26) Ashok, B.; Muthukumar, M.; Russell, T. P. Confined Thin Film Diblock Copolymer in the Presence of an Electric Field. *J. Chem. Phys.* **2001**, *115* (3), 1559–1564. <https://doi.org/10.1063/1.1380710>.
- (27) Olszowka, V.; Hund, M.; Kuntermann, V.; Scherdel, S.; Tsarkova, L.; Böker, A. Electric Field Alignment of a Block Copolymer Nanopattern: Direct Observation of the Microscopic Mechanism. *ACS Nano* **2009**, *3* (5), 1091–1096. <https://doi.org/10.1021/nn900081u>.
- (28) Gopinadhan, M.; Choo, Y.; Kawabata, K.; Kaufman, G.; Feng, X.; Di, X.; Rokhlenko, Y.; Mahajan, L. H.; Ndaya, D.; Kasi, R. M.; Osuji, C. O. Controlling Orientational Order in Block Copolymers Using Low-Intensity Magnetic Fields. *Proc. Natl. Acad. Sci.* **2017**, *114* (45), E9437–E9444. <https://doi.org/10.1073/pnas.1712631114>.
- (29) Rokhlenko, Y.; Gopinadhan, M.; Osuji, C. O.; Zhang, K.; O’Hern, C. S.; Larson, S. R.; Gopalan, P.; Majewski, P. W.; Yager, K. G. Magnetic Alignment of Block Copolymer Microdomains by Intrinsic Chain Anisotropy. *Phys. Rev. Lett.* **2015**, *115* (25), 258302. <https://doi.org/10.1103/PhysRevLett.115.258302>.
- (30) Tran, H.; Gopinadhan, M.; Majewski, P. W.; Shade, R.; Steffes, V.; Osuji, C. O.; Campos, L. M. Monoliths of Semiconducting Block Copolymers by Magnetic Alignment. *ACS Nano* **2013**, *7* (6), 5514–5521. <https://doi.org/10.1021/nn401725a>.
- (31) Majewski, P. W.; Yager, K. G. Latent Alignment in Pathway-Dependent Ordering of Block Copolymer Thin Films. *Nano Lett.* **2015**, *15* (8), 5221–5228. <https://doi.org/10.1021/acs.nanolett.5b01463>.
- (32) Angelescu, D. E.; Waller, J. H.; Adamson, D. H.; Deshpande, P.; Chou, S. Y.; Register, R. A.; Chaikin, P. M. Macroscopic Orientation of Block Copolymer Cylinders in Single-Layer Films by Shearing. *Adv. Mater.* **2004**, *16* (19), 1736–1740. <https://doi.org/10.1002/adma.200400643>.
- (33) Nikoubashman, A.; Davis, R. L.; Michal, B. T.; Chaikin, P. M.; Register, R. A.; Panagiotopoulos, A. Z. Thin Films of Homopolymers and Cylinder-Forming Diblock

- Copolymers under Shear. *ACS Nano* **2014**, *8* (8), 8015–8026. <https://doi.org/10.1021/nn502068e>.
- (34) Qiang, Z.; Zhang, Y.; A. Groff, J.; A. Cavicchi, K.; D. Vogt, B. A Generalized Method for Alignment of Block Copolymer Films: Solvent Vapor Annealing with Soft Shear. *Soft Matter* **2014**, *10* (32), 6068–6076. <https://doi.org/10.1039/C4SM00875H>.
- (35) Gottlieb, E. R.; Guliyeva, A.; Epps, T. H. I. From Lab to Fab: Enabling Enhanced Control of Block Polymer Thin-Film Nanostructures. *ACS Appl. Polym. Mater.* **2021**, *3* (9), 4288–4303. <https://doi.org/10.1021/acsapm.1c00680>.
- (36) Weller, D. W.; Galuska, L.; Wang, W.; Ehlenburg, D.; Hong, K.; Gu, X. Roll-to-Roll Scalable Production of Ordered Microdomains through Nonvolatile Additive Solvent Annealing of Block Copolymers. *Macromolecules* **2019**, *52* (13), 5026–5032. <https://doi.org/10.1021/acs.macromol.9b00772>.
- (37) Leniart, A. A.; Pula, P.; Sitkiewicz, A.; Majewski, P. W. Macroscopic Alignment of Block Copolymers on Silicon Substrates by Laser Annealing. *ACS Nano* **2020**, *14* (4), 4805–4815. <https://doi.org/10.1021/acsnano.0c00696>.
- (38) Kim, G.; Libera, M. Morphological Development in Solvent-Cast Polystyrene–Polybutadiene–Polystyrene (SBS) Triblock Copolymer Thin Films. *Macromolecules* **1998**, *31* (8), 2569–2577. <https://doi.org/10.1021/ma971349i>.
- (39) Kim, S. H.; Misner, M. J.; Xu, T.; Kimura, M.; Russell, T. P. Highly Oriented and Ordered Arrays from Block Copolymers via Solvent Evaporation. *Adv. Mater.* **2004**, *16* (3), 226–231. <https://doi.org/10.1002/adma.200304906>.
- (40) Hu, H.; Singer, J. P.; Osuji, C. O. Morphology Development in Thin Films of a Lamellar Block Copolymer Deposited by Electrospray. *Macromolecules* **2014**, *47* (16), 5703–5710. <https://doi.org/10.1021/ma500376n>.
- (41) Hu, H.; Rangou, S.; Kim, M.; Gopalan, P.; Filiz, V.; Avgeropoulos, A.; Osuji, C. O. Continuous Equilibrated Growth of Ordered Block Copolymer Thin Films by Electrospray Deposition. *ACS Nano* **2013**, *7* (4), 2960–2970. <https://doi.org/10.1021/nn400279a>.
- (42) Park, S. H.; Lei, L.; D'Souza, D.; Zipkin, R.; DiMartini, E. T.; Atzampou, M.; Lallow, E. O.; Shan, J. W.; Zahn, J. D.; Shreiber, D. I.; Lin, H.; Maslow, J. N.; Singer, J. P. Efficient Electrospray Deposition of Surfaces Smaller than the Spray Plume. *Nat. Commun.* **2023**, *14* (1), 4896. <https://doi.org/10.1038/s41467-023-40638-7>.
- (43) Toth, K.; Osuji, C. O.; Yager, K. G.; Doerk, G. S. High-Throughput Morphology Mapping of Self-Assembling Ternary Polymer Blends. *RSC Adv.* **2020**, *10* (69), 42529–42541. <https://doi.org/10.1039/D0RA08491C>.
- (44) Toth, K.; Bae, S.; Osuji, C. O.; Yager, K. G.; Doerk, G. S. Film Thickness and Composition Effects in Symmetric Ternary Block Copolymer/Homopolymer Blend Films: Domain Spacing and Orientation. *Macromolecules* **2021**, *54* (17), 7970–7986. <https://doi.org/10.1021/acs.macromol.1c01032>.
- (45) Hu, H.; Choo, Y.; Feng, X.; Osuji, C. O. Physical Continuity and Vertical Alignment of Block Copolymer Domains by Kinetically Controlled Electrospray Deposition. *Macromol. Rapid Commun.* **2015**, *36* (13), 1290–1296. <https://doi.org/10.1002/marc.201500099>.
- (46) Phillip, W. A.; Hillmyer, M. A.; Cussler, E. L. Cylinder Orientation Mechanism in Block Copolymer Thin Films Upon Solvent Evaporation. *Macromolecules* **2010**, *43* (18), 7763–7770. <https://doi.org/10.1021/ma1012946>.
- (47) Bishop, J. E.; Routledge, T. J.; Lidzey, D. G. Advances in Spray-Cast Perovskite Solar Cells. *J. Phys. Chem. Lett.* **2018**, *9* (8), 1977–1984. <https://doi.org/10.1021/acs.jpcllett.8b00311>.

- (48) Yuan, J.; Bi, C.; Wang, S.; Guo, R.; Shen, T.; Zhang, L.; Tian, J. Spray-Coated Colloidal Perovskite Quantum Dot Films for Highly Efficient Solar Cells. *Adv. Funct. Mater.* **2019**, *29* (49), 1906615. <https://doi.org/10.1002/adfm.201906615>.
- (49) Alanazi, T. I. Current Spray-Coating Approaches to Manufacture Perovskite Solar Cells. *Results Phys.* **2023**, *44*, 106144. <https://doi.org/10.1016/j.rinp.2022.106144>.
- (50) Brassat, K.; Kool, D.; Nallet, C. G. A.; Lindner, J. K. N. Understanding Film Thickness-Dependent Block Copolymer Self-Assembly by Controlled Polymer Dewetting on Prepatterned Surfaces. *Adv. Mater. Interfaces* **2020**, *7* (1), 1901605. <https://doi.org/10.1002/admi.201901605>.
- (51) Deegan, R. D.; Bakajin, O.; Dupont, T. F.; Huber, G.; Nagel, S. R.; Witten, T. A. Capillary Flow as the Cause of Ring Stains from Dried Liquid Drops. *Nature* **1997**, *389* (6653), 827–829. <https://doi.org/10.1038/39827>.
- (52) Man, X.; Doi, M. Ring to Mountain Transition in Deposition Pattern of Drying Droplets. *Phys. Rev. Lett.* **2016**, *116* (6), 066101. <https://doi.org/10.1103/PhysRevLett.116.066101>.
- (53) Choi, M.-J.; Kim, Y.; Lim, H.; Alarousu, E.; Adhikari, A.; Shaheen, B. S.; Kim, Y. H.; Mohammed, O. F.; Sargent, Edward. H.; Kim, J. Y.; Jung, Y. S. Tuning Solute-Redistribution Dynamics for Scalable Fabrication of Colloidal Quantum-Dot Optoelectronics. *Adv. Mater.* **2019**, *31* (32), 1805886. <https://doi.org/10.1002/adma.201805886>.
- (54) Bellini, B.; Willard, J. R.; Cetindag, S.; Tsai, E. H. R.; Li, R.; Kisslinger, K.; Kumar, S. K.; Doerk, G. S. Assembling Vertical Block Copolymer Nanopores via Solvent Vapor Annealing on Homopolymer-Functionalized Substrates. *ACS Appl. Mater. Interfaces* **2024**, *16* (27), 35541–35553. <https://doi.org/10.1021/acsami.4c05715>.
- (55) Subramanian, A.; Doerk, G.; Kisslinger, K.; Yi, D. H.; Grubbs, R. B.; Nam, C.-Y. Three-Dimensional Electroactive ZnO Nanomesh Directly Derived from Hierarchically Self-Assembled Block Copolymer Thin Films. *Nanoscale* **2019**, *11* (19), 9533–9546. <https://doi.org/10.1039/C9NR00206E>.
- (56) Majewski, P. W.; Yager, K. G. Reordering Transitions during Annealing of Block Copolymer Cylinder Phases. *Soft Matter* **2015**, *12* (1), 281–294. <https://doi.org/10.1039/C5SM02441B>.
- (57) Cavicchi, K. A.; Russell, T. P. Solvent Annealed Thin Films of Asymmetric Polyisoprene–Polylactide Diblock Copolymers. *Macromolecules* **2007**, *40* (4), 1181–1186. <https://doi.org/10.1021/ma061163w>.
- (58) Bai, W.; Yager, K. G.; Ross, C. A. In Situ Characterization of the Self-Assembly of a Polystyrene–Polydimethylsiloxane Block Copolymer during Solvent Vapor Annealing. *Macromolecules* **2015**, *48* (23), 8574–8584. <https://doi.org/10.1021/acs.macromol.5b02174>.
- (59) Doerk, G. S.; Li, R.; Fukuto, M.; Rodriguez, A.; Yager, K. G. Thickness-Dependent Ordering Kinetics in Cylindrical Block Copolymer/Homopolymer Ternary Blends. *Macromolecules* **2018**, *51* (24), 10259–10270. <https://doi.org/10.1021/acs.macromol.8b01773>.
- (60) Pula, P.; Leniart, A.; Majewski, P. W. Solvent-Assisted Self-Assembly of Block Copolymer Thin Films. *Soft Matter* **2022**, *18* (21), 4042–4066. <https://doi.org/10.1039/D2SM00439A>.
- (61) Hao, J.; Wang, Z.; Wang, Z.; Yin, Y.; Jiang, R.; Li, B.; Wang, Q. Self-Assembly in Block Copolymer Thin Films upon Solvent Evaporation: A Simulation Study. *Macromolecules* **2017**, *50* (11), 4384–4396. <https://doi.org/10.1021/acs.macromol.7b00200>.
- (62) Paradiso, S. P.; Delaney, K. T.; García-Cervera, C. J.; Ceniceros, H. D.; Fredrickson, G. H. Block Copolymer Self Assembly during Rapid Solvent Evaporation: Insights into Cylinder Growth and Stability. *ACS Macro Lett.* **2014**, *3* (1), 16–20. <https://doi.org/10.1021/mz400572r>.

- (63) Dreyer, O.; Ibbeken, G.; Schneider, L.; Blagojevic, N.; Radjabian, M.; Abetz, V.; Müller, M. Simulation of Solvent Evaporation from a Diblock Copolymer Film: Orientation of the Cylindrical Mesophase. *Macromolecules* **2022**, *55* (17), 7564–7582. <https://doi.org/10.1021/acs.macromol.2c00612>.
- (64) Zhang, X.; Douglas, J. F.; Jones, R. L. Influence of Film Casting Method on Block Copolymer Ordering in Thin Films. *Soft Matter* **2012**, *8* (18), 4980–4987. <https://doi.org/10.1039/C2SM07308K>.
- (65) Liapis, A. C.; Rahman, A.; Black, C. T. Self-Assembled Nanotextures Impart Broadband Transparency to Glass Windows and Solar Cell Encapsulants. *Appl. Phys. Lett.* **2017**, *111* (18), 183901. <https://doi.org/10.1063/1.5000965>.
- (66) Russell, S. T.; Bae, S.; Subramanian, A.; Tiwale, N.; Doerk, G.; Nam, C.-Y.; Fukuto, M.; Yager, K. G. Priming Self-Assembly Pathways by Stacking Block Copolymers. *Nat. Commun.* **2022**, *13* (1), 6947. <https://doi.org/10.1038/s41467-022-34729-0>.
- (67) Liu, Y.; Ji, S. Determination of the Maximum Thickness for Directed Self-Assembly of Cylinder-Forming PS-*b*-PMMA Films on Chemical Patterns. *Mol. Syst. Des. Eng.* **2018**, *3* (2), 342–347. <https://doi.org/10.1039/C7ME00101K>.
- (68) Ji, S.; Liu, C.-C.; Liu, G.; Nealey, P. F. Molecular Transfer Printing Using Block Copolymers. *ACS Nano* **2010**, *4* (2), 599–609. <https://doi.org/10.1021/nn901342j>.
- (69) Singh, G.; Batra, S.; Zhang, R.; Yuan, H.; Yager, K. G.; Cakmak, M.; Berry, B.; Karim, A. Large-Scale Roll-to-Roll Fabrication of Vertically Oriented Block Copolymer Thin Films. *ACS Nano* **2013**, *7* (6), 5291–5299. <https://doi.org/10.1021/nn401094s>.
- (70) Modi, A.; Bhaway, S. M.; Vogt, B. D.; Douglas, J. F.; Al-Enizi, A.; Elzatahry, A.; Sharma, A.; Karim, A. Direct Immersion Annealing of Thin Block Copolymer Films. *ACS Appl. Mater. Interfaces* **2015**, *7* (39), 21639–21645. <https://doi.org/10.1021/acsami.5b06259>.
- (71) Zhou, C.; Segal-Peretz, T.; Oruc, M. E.; Suh, H. S.; Wu, G.; Nealey, P. F. Fabrication of Nanoporous Alumina Ultrafiltration Membrane with Tunable Pore Size Using Block Copolymer Templates. *Adv. Funct. Mater.* **2017**, *27* (34), 1701756. <https://doi.org/10.1002/adfm.201701756>.
- (72) Lang, R. J. Ultrasonic Atomization of Liquids. *J. Acoust. Soc. Am.* **1962**, *34* (1), 6–8. <https://doi.org/10.1121/1.1909020>.

# For Table of Contents Only

